COMPUTER MODELLING OF TRANSITION METAL SULPHIDE (FeS_2)

A thesis presented

BY

MOFUTI AMOS MEHLAPE

SUBMITTED

TO THE

FACULTY OF SCIENCE, HEALTH AND AGRICULTURE

UNIVERSITY OF LIMPOPO,
TURFLOOP CAMPUS

IN FULFILMENT OF MASTER OF SCIENCE

DEGREE

IN

SUBJECT

OF

PHYSICS

SUPERVISOR: PROF. P.E. NGOEPE
Co-SUPERVISOR: PROF. S.C. PARKER

[2007]

Declaration

I declare that the dissertation hereby submitted to the University of Limpopo (Turfloop Campus) for the degree of Master of Science has not been previously submitted by me and that this is my own work and that all quotations and paraphrases from other sources have been duly acknowledged by footnotes or endnotes and in the bibliography.

Signature of the Author: ----------

Mofuti A. Mehlape

Abstract

The aim of this thesis is to study the structure and reactivity of FeS2 (pyrite).The transition metal sulphide, FeS_2 crystallizes into cubic (pyrite) and orthorhombic (marcasite), is an important member of the sulphides minerals.

The adjusted interatomic potentials were used for both energy minimization and molecular dynamics to study the surfaces and the bulk structure of pyrite. We also modelled the polymorph of pyrite, marcasite. With energy minimization we calculated the surface energies of the surfaces {100}, {110}, {111} and {210}. They revealed that {100} surface is the most stable surface. When we compared the surface energies calculated from the original potentials and the adjusted potentials, it is clear that the adjusted potentials improve the stability of the surfaces. It was also revealed that water stabilizes the surfaces, since the surface energies decreases when hydrated. Molecular dynamics (MD) was used to see the effect of temperature on the surfaces. To analyze our results we used the MD properties, namely, radial distribution functions (RDFs), diffusion coefficient and mean squared displacement (MSD). It was shown that as we increase the temperature both the bulk and the surfaces reach the molten phase. The melting point of the bulk is high than that of surfaces. Again molecular dynamics was used to study the nanocrystals of pyrite. We investigated the aggregation process of the pyrite nanoparticles. With the help of the RDF, it was revealed that the particles adopt a near amorphous structure when aggregated. We considered the effect of the crystal size on the solid/water interface. We modelled a pyrite nanoparticle in vacuum and immersed in water. The nanoparticle undergoes a phase change in vacuum, but in the presence of water, the pyrite structure was stabilized.

Acknowledgements

I would like to thank my supervisor, Professor P.E. Ngoepe and co-supervisor Professor S.C. Parker, for the support, patience and guidance throughout this project. Thanks must also go to my colleagues at the Materials Modelling Centre, Dr D.J. Cooke and members of the The Parker group at University of Bath, UK.

I would like to acknowledge the National Research Foundation (South Africa), and the Royal Society (UK) for their financial support.

Most of all I would like to thank my family, my mother Henriettah Moore Mehlape, my sisters, Stella Mosima Madaba and her family and Maite Maria Mehlape for the support and patience throughout my study. Ke leboga go menagane.

Dedication

I dedicate this thesis to the memory of my late father Mr. Matome Robert Mehlape

Table of Contents

List of Figures

List of Tables

Chapter 1

Introduction

1.1 General Background

The transition metal sulphides are a major group of minerals [Sithole et al, 1999]. Metal sulphides minerals are of vast industrial and economic importance; this is because they are the main source of metals such as zinc, copper and lead [Muscat et al, 2002]. Pyrite is commonly associated as a gangue mineral with several base metal sulphides such as copper, lead, and zinc [Rath et al, 2000]. In this project we are interested in the iron sulphide (FeS_2).

Pyrite has been a subject of several studies for many years. As one of the most common minerals on earth, it has many applications and investigation of its surface structure is a significant part of developing for example, solar cells or ore processing methods. Recently, sulphide minerals have also been studied among space research because of their appearance, for example, in meteoric stones and cometary dust. Oxidation of pyrite has important environmental aspects. It is a large problem in mining areas leading to the formation of sulphuric acid [Mattila et al, 2004]. Pyrite (FeS_2) has received attention in recent years owing to its potential application as a useful material for solar energy applications, as a cathode in high-energy-density batteries and as depolarizer anode for hydrogen production [Chen et al, 1994].

Figure 1.1: A rock containing a brassy yellow pyrite.

Figure 1.1 shows a rock containing a brassy yellow pyrite. Pyrite is the classic "Fool's Gold". There are other shiny brassy yellow minerals, but pyrite is by far the most common and the most often mistaken for gold. Whether it is the golden look or something else, pyrite is a favourite among rock collectors.

The pyrite-type transition metal disulphides MS_2 with M = Fe, Mn, Co, Ni, Zn, Ru have long been attracting scientific and technological interest because of a broad range of electronic, magnetic, and optical properties. Our main focus in this work, FeS_2 is a van Vleck paramagnet superconductor, ZnS_2 is a wide–band-gap diamagnet insulator, CoS_2 is a ferromagnetic metal, CuS_2 becomes superconducting, NiS_2 is a

paramagnetic Mott-Hubard insulator and MnS_2 is an anti-ferromagnetic semiconductor [Eyert et al., 1998 and Sithole, 2000].

1.2 Literature Review

There has been a lot of studies done before of iron sulphide (FeS_2). These sections look at the previous studies that have been done before of Fe S_2, using experimental studies and computer simulation studies.

1.2.1 Experimental Studies

A lot of experimental techniques have been used to study FeS_2. Huang et al (1993) reported an electrolyte electro reflectance (EER) study of synthetic pyrite FeS_2 single crystals. They found that EER exhibits derivative-like structures in the vicinity of the interband transitions. Chen et al (1994) used the photoconductivity measurements of synthetic pyrite FeS_2 single crystals at low temperature to study the impurity and defect-related photo response peaks below the band edge. They found that at temperature below 100 K, there are several features on the low-energy side of the photoconductivity spectra. Rosso et al (1999) studied the interaction with gaseous O_2 and H_2O and their mixture with clean of (100) surfaces of pyrite (FeS_2) were investigated in ultra-high vacuum using scanning tunneling microscopy and spectroscopy (STM-STS) and ultraviolet photoelectron spectroscopy (UPS). They follow these with the surface defects and self-diffusion of the pyrite (100) using an ultra-high vacuum scanning tunneling microscopy and also theoretical modeling study Rosso et al (2000). Photoelectron spectroscopy was also used by Elsetinow et al (2000) to investigate the oxidation of (100) and (111) surfaces of pyrite. Descostes et al (2004) studied the oxidation pyrite in aqueous solutions using the Scanning electron

microscopy to remove any fine particles adhering to the grain surfaces, and X-ray photoelectron spectroscopy (XPS) was used to control the surface purity, and X-ray diffraction was also used to confirm the absence of any accessory minerals. Mattila et al (2004) studied oxidized mineral pyrite FeS_2 using the synchrotron exited photoelectron spectroscopy (XPS). The other experimental studies where done by Meng et al (2003) using X-Ray Diffraction (XRD). They looked at the structural, optical and electrical properties of polycrystalline pyrite (FeS_2) films. They found that pyrite particles formed at 673 K reveal an aggregate Scanning Electron Microscope (SEM) morphology evolved from some transitional iron sulphides. Another SEM and XRD study was by Wan et al (2003), they studied the effect of the crystal structure on the optical and electrical properties of pyrite FeS_2 films produced by thermally sulfurizing iron films at various temperatures. Their results indicate that the crystal structure and some related factors, such as the crystallization and the stoichiometry, influence the optical and electrical performances of the pyrite films. Wu et al. (2004) studied pyrite FeS_2 by XRD, a Rietveld refinement method, SEM and ultraviolet-visible (UV-VIS) spectrophotometry. With the XRD and Rietveld structure refinement indicated that the sample structure is a typical AB_2 cubic of space group Pa3 with the lattice constant $a = 5.4151\mathring{A}$ and a Wyckoff parameter $u = 0.3868$. SEM showed that the polycrystalline pyrite was well crystallized. One of the recent experimental studies was by Chen et al (2005), they synthesized cubic FeS_2 crystallites and their Optical and Electrochemical properties via a single source approach, and the sample was characterized by XRD, Tunneling Electron Microscope (TEM) and Field Emission Electron Microscope (FESEM). The optical properties of the as-prepared FeS_2 reveal that there exists a red shift compared with that of bulk materials. The electrochemical properties of FeS_2 demonstrate that it delivers a large

discharge capacity. It was also found that the reaction temperature is of importance to the formation of cubic FeS_2 crystallites. The surface Brillouin scattering was used to study the variation of the velocities of the Rayleigh surface acoustic wave (RSAW) and the high frequency pseudo-SAW (HFPSAW) with azimuthal angle on the (110) surface of iron pyrite (FeS_2) over the temperature range 293 to 573K (Tlali et al, 2004).

One of our aims in this thesis is to look at the nanoparticles of pyrite and perhaps other transitional metal sulphides. Recently the metal nanocrystals have been getting a lot of attention due to fact that they have interesting optical and electronic properties. Metal colloidal nanoparticles are becoming increasingly important in a variety of scientific fields, like in molecular spectroscopy applications, the interest stems from the significant improvement in the detection of the Raman signal from molecules adsorbed on roughened metal surfaces [Mock et al, 2002]. Nanometer processing is receiving considerable interest from variety of communities, including those from microelectronics and advanced materials [Zachariah and Carrier, 1996]. There has been an increasing emphasis on developing and manipulating nanoscale materials, precise control over the size, chemical identity and shape of nanoparticles must be achieved to further develop innovative nanoscale materials with novel applications [Fullerton and Maranas, 2005]. As such shape and size on materials are very important and since the nanocrystals have attracted a lot of interest and everything needs to be small and better than the last device. It has been cited in a publication by Sayle and Parker (2003) that as the size of a material reduces to the nanometer scale, the structure and properties change uniquely in comparison with those of the bulk. Pyrite is an important step in a number of industrial processes such as e.g. the roasting of pyritiferous gold-containing ores, the production of sulphuric acid, high-density

batteries, precursors for the synthesis of superconductors, materials for photoelectrolysis, solar energy materials [Chin et al, 2005 and Eneroch and Koch, 2003]. Many important industrial processes produce nanoparticles either as unwanted byproducts or as desired end products. Nanoparticles can form in the process equipment used to fabricate microelectronic devices and ruin the devices if deposited on their surface. Novel catalysts and materials can be prepared using nanopartilces. (Higgins et al. 2002). Iron sulphide nanoparticles have a significant potential for applications in many areas, for example they may be used in electrochemical reaction in the investigation of life origin [Chin et al, 2005].

1.2.2 Computer Simulation Studies

Computer Simulation techniques have also been used to study FeS_2. Zeng and Holzwarth (1994) used the self-consistent density-functional theory (DFT) comparing the local-density-approximation (LDA) and generalised-gradient-approximation (GGA) forms of the exchange-correlation functional to study the electronic structure and equilibrium geometry of the pyrite form of FeS2. They also obtained the same results with another pyrite structure RuS2. Hung et al (2002) performed the DFT calculations. The other DFT study of FeS2 was by Hung et al (2003), they used the method with plane wave-pseudopotentials to study the structure and properties of a model xanthate molecule ($HOCS^-_2$) and its adsorption characteristics on the pyrite FeS_2 (110) and (111) surfaces. In this study we look at the adsorption of water on the FeS_2 surfaces. Qiu G. et al (2004) studied the geometric and electronic structures of FeS_2 (100) surface by quantum-mechanical calculation using total-energy pseudopotential code, CASTEP. They found that {100} surface is very stable and does not give any significant geometric relaxation. Cai and Philpott (2004) studied the

electronic structure of bulk and (001) surface layers of pyrite FeS_2. They used a modern ab initio pseudo-potential method.

1.3 Structural Aspects

1.3.1. FeS_2 (Pyrite)

Pyrite is cubic with cell edge a ~ 5.42 Å; Fe atoms are at the corners and face centers of the cube, and S atoms are arranged in 'dumb-bell' pairs centered at the mid-points of the cube edges and at the cube's body center, the structure of pyrite shown in figure 1.2. The four S-S joins are respectively parallel to four non-intersecting body diagonal directions. Each iron atom is surrounded by six sulphur atoms at the corners of an octahedron, shown in Figure 1.2 and each sulphur atom is equidistant from three iron atoms which form a triangular planar group to one side. If the mid-points of sulphur pairs are considered, these are in arrangement of cubic close packing, and a Fe atom lies in each of the octahedral holes. Compared with many other sulphides the structure of pyrite is very densely packed. Both NiS_2 (vaesite, a = 5.679 Å) and CoS_2 (cattierite, a = 5.535 Å) posses the pyrite structure, and the substitution of Fe by Ni or Co in pyrite increases the cell edge [Deer et al, 1992]. The cubic pyrite structure can be considered as a derivative of the face-centered rock salt structure, NaCl, where $(S_2)^{-2}$ occupies the Cl sites and Fe^{2+} occupies Na sites.

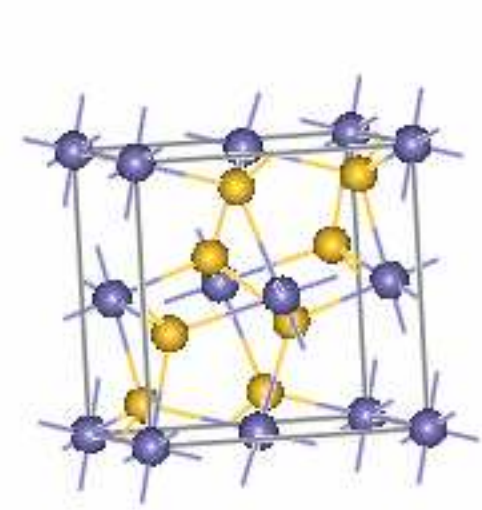

Figure 1.2: Cubic structure of pyrite, purple atoms represent iron (Fe) and yellow atoms represent sulphur (S).

The structure may be viewed as consisting of 12 interpenetrating simple cubic sublattices. Four of these have iron atoms located at the lattice sites, and the other eight have sulphur atoms. The sulphur atoms are positioned such that the line joining adjacent sulphur pairs is aligned along one of the equivalent <111> directions [Verble and Wallis, 1969] (see Figure 1.3). Table 1.1 shows the positions of atoms in the pyrite unit cell.

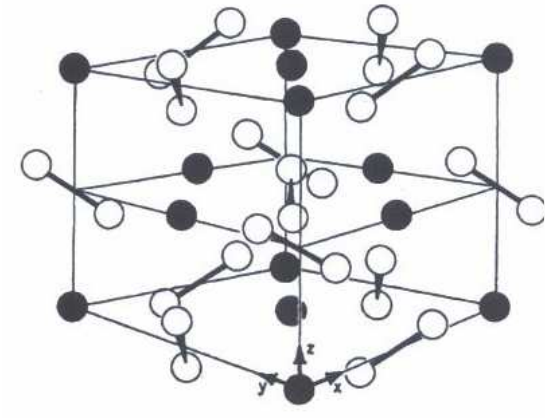

Figure 1.3: Cyrstal structure and primitive cell of pyrite. Black spheres represent iron atoms, while the white spheres represent the sulphur atoms.

Table 2.1: Positions of atoms in the pyrite unit cell. The parameter u has the value 0.386 for FeS_2 (Verble and Wallis, 1969)

Fe		S	
κ	Coordinates	κ	Coordinates
1	(0, 0, 0)	5	(u,u,u)
2	$(0, \frac{1}{2}, \frac{1}{2})$	6	$(-u,-u,-u)$
3	$(\frac{1}{2}, 0, \frac{1}{2})$	7	$(u-\frac{1}{2},-u+\frac{1}{2},-u)$
4	$(\frac{1}{2}, \frac{1}{2}, 0)$	8	$(-u+\frac{1}{2},u-\frac{1}{2},u)$
		9	$(-u,u-\frac{1}{2},-u+\frac{1}{2})$
		10	$(u,-u+\frac{1}{2},u-\frac{1}{2})$
		11	$(-u+\frac{1}{2},-u,u-\frac{1}{2})$
		12	$(u-\frac{1}{2},u,-u+\frac{1}{2})$

1.3.2. FeS_2 (Marcasite)

The mineral marcasite is a dimorph of pyrite. It is orthorhombic with a ~ 4.45 Å, b ~ 5.42 Å, c ~ 3.39 Å, Z =2, space group Pmnn. As in pyrite, iron is octahedrally coordinated by sulphur, but the sulphur pairs are in layers with hexagonal rather than cubic stacking and the octahedra share edges rather than corners. The structure of

marcasite projected on (101) is similar to that of pyrite on (100). $a_{pyrite} \sim b_{marcasite}$ and a_{pyrite} is approximately equal to the a – c diagonal of marcasite cell, and intergrowths are formed with these faces in common [Deer et al, 1992]. The orthorhombic marcasite structure is shown in Figure 1.4.

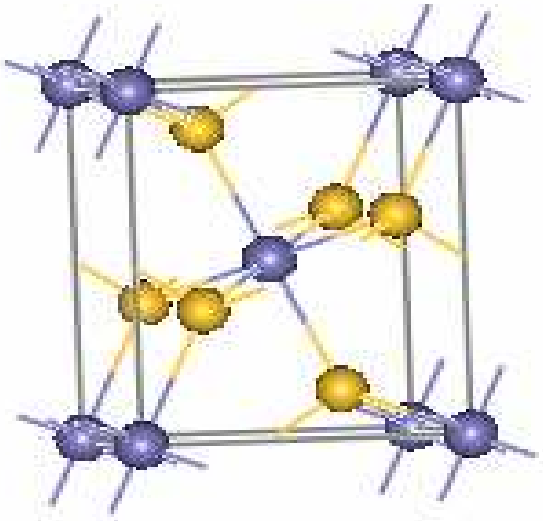

Figure 1.4: Orthorhombic structure of marcasite

1.4. Rationale of the Study

Metal sulphide minerals are of vast industrial and economic importance, since they are the main source of metals such as zinc, copper and lead [Muscat et al, 2002]. In this project we are interested in the iron sulphide (FeS_2). Of the sulphide minerals, pyrite structured FeS_2 is the most common form, and serves as a useful model system for understanding the chemical and physical properties of this class of minerals [Muscat et al, 2002]. The FeS_2 structure, which crystallizes into cubic (pyrite) and orthorhombic (marcasite), is an important member of the sulphide minerals. Pyrite, (FeS_2), (also known as the fool's gold) is the most common sulfide found in many environments. It is a common accessory mineral in igneous, sedimentary and metamorphic rocks. A brass-coloured mineral, FeS_2, occurs widely as an iron ore in

producing sulfur dioxide for sulfuric acid. The second most important industrial chemical, sulfuric acid (water is first), is made from pyrite [http://www.gamineral.org/pyrite.htm].

Many aspects of pyrite surface chemistry and reactivity are difficult to explain or understand, despite a considerable volume of research. The study of pyrite has been mainly driven by its importance in aqueous environment systems and by its usefulness as a photovoltaic material. Pyrite often coexists in ores of other desired minerals and its behaviour in mineral deposits in various aqueous environment concern. Pyrite-rich deposits are often mined for metals such as Au, Ag, Cu, Zn and Pb, which are typically present as impurities in pyrite or occur in sulphide minerals as chalcopyrite ($CuFeS_2$), Sphalerite (ZnS) and Galena (PbS) (Baker and Banfield, 2003).

1.5. Objective of the Study

This study is based on atomistic simulation of the iron sulphide. We use molecular dynamics (MD), which is coupled with the interatomic potentials. The potentials that we use in this study were derived by [Sithole, 2000]. These potentials were adjusted to give a better S-S intramolecular distance. In our calculations we used the MD code called DL_POLY. The NPT and NVT ensembles will be used for the bulk and the low index surfaces, namely {100}, {110}, {111} and {210}. The structure of the bulk and surfaces will be determined at different temperatures from the radial distribution functions (rdfs), diffusion coefficients and mean squared displacement (MSD). With these parameters we are able to determine the melting temperature of the bulk and the surfaces. We also look at the effect of water on the surfaces, by comparing the calculated surface energies of the pure surfaces and the hydrated surfaces.

MD will be used to study the nanoparticles of the {100} surface of pyrite, together with the aggregation process of pyrite clusters. We will also look at the effect of water on the structure of a pyrite nanoparticle.

1.5. Outline of the Study

Chapter 1 contains the general background of the transition metal sulphide, FeS_2. The major experimental and computational studies of pyrite are reviewed. The structural aspects of the FeS_2 are discussed in this chapter. The objective and rationale of the study are also outlined.

Chapter 2 discusses the theoretical aspects and methodology used throughout this work, in particular the computational techniques, such as energy minimisation and molecular dynamics.

In Chapter 3, the potential model is discussed and the pyrite potentials used in this work are also explained.

In Chapters 4 and 5 we present the main results obtained in this work. Chapter 4 gives the effect of temperature and water on the surfaces of pyrite, using both the energy minimisation and molecular dynamics techniques. With energy minimisation we reveal that the {100} surface is the most stable surface in both the dry and hydrated surfaces. We show that water stabilises the surfaces, since the surface energy decreases when hydrated. Chapter 5 we study the aggregation of pyrite nanoparticles and the effect of water on the nanoparticle of pyrite. In Chapter 6 we give conclusion and future work.

Chapter 2

Theoretical Studies and Methodology

2.1. Atomistic Simulation

Atomistic computer modelling techniques now play a major role in both physical and biological sciences [Catlow, 1997]. An atomistic simulation is now able to model the structure of mineral surfaces at the atomic level and is a valuable tool for interpreting and predicting surface structures [De Leeuw and Parker, 1999 Parker et al, 1999]. The atomistic simulations are based on the Born model of ionic solids [Born and Huang, 1954], in which the ions interact *via* long-range electrostatic forces and short-range forces. The value of atomistic simulations in the earth and materials sciences lies in demonstrating the mechanisms of atomistic procedures, and extending this capability to evaluate material properties to regimes where direct laboratory measurements are difficult or impossible to perform [Fisler et al., 2000]. Atomistic models are limited to small system sizes. The major disadvantage is their inability to explicitly model electronic properties. This problem is overcome by the use of electronic structure calculation Density functional theory (DFT). The advantage of atomistic simulation is the computer time. We are able to model bigger system for a short period of time as compared to DFT. Energy minimization allows us to evaluate the most stable configurations and molecular dynamics provides the effect of temperature on the system. These techniques are discussed in the following sections.

2.1.1 Energy Minimisation

Energy minimisation allows us to evaluate energy of a system by adjusting the atom positions until a minimum energy configuration of the atoms is obtained. In this work we used energy minimisation throughout to calculate the energies and equilibrium structures of the bulk and surfaces of pyrite. For energy minimisation we use the code METADISE (minimum energy techniques applied to dislocations, interfaces, surface energies) [Watson et al, 1996], and it is a program that uses energy minimisation to calculate the structure of systems periodic in various dimensions (zero nanoparticles, one dislocations, two surfaces and three bulk). The advantage of energy minimisation is that (for a systems of a few hundred atoms) it does not demand computationally, so it can be used to scan a range of possible configurations. The drawback of energy minimisation are that for large systems the inversion of the matrix of second order derivatives becomes prohibitively expensive, something which the ever increasing power of computers and techniques such as molecular dynamics go some way to negating and that it does not take account of the vibrational properties of the system. There is no representation of temperature in the simulated system however this effect will be small for ideal solid systems.

The lowest energy configuration is found by using an iterative procedure to adjust the atom positions until the interaction energy is minimised. The calculated interaction energy should be the minimum interaction energy of the system, i.e., the system must be at its mechanical equilibrium and there should be no residual stresses. However, this is rarely the case on setting up a simulation cell and hence the interaction energy needs to be minimized so as to remove these residual stresses. There are two ways of achieving this: Firstly, via a constant volume or constant area minimization, where the cell dimensions are kept fixed but the position of the ions can be modified. Secondly, by means of a constant pressure minimization where both the cell dimensions and the

ions can relax, i.e., forces on the atoms and the cell dimensions are both removed [Kerisit PhD, 2005].

The Newton-Raphson variable matrix method has been employed for energy minimisation calculations throughout this work. This minimisation procedure optimises the energy of the systems modelled with the potential energy.

2.1.2 Molecular Dynamics

Molecular dynamics simulation is a computational technique used to study the motions of atoms in a given system (e.g., a solid material or a solid solution could equally be liquids and gases) in order to understand and predict the structural , dynamic, kinetic, and /or equilibrium properties at a chosen conditions (e.g., compositions, temperatures, and pressures) [Zhang and Banfield, 2004]. Molecular dynamics (MD) is a powerful method for exploring the structure of solids, liquids and gases. It is a modern method which requires electronic computers. Molecular Dynamics simulations are in many respects very similar to real experiments. When we perform a real experiment, we proceed as follows. We prepare a sample of the material that we wish to study. We connect this sample to a measuring instrument (e.g. a thermometer, manometer, or viscometer), and we measure the property of interest during a certain time interval. If our measurements are subject to statistical noise (as most measurements are), then the longer we average, the more accurate our measurement becomes. In Molecular Dynamics simulation, we follow exactly the same approach. First, we prepare a sample: we select a model system consisting of N particles and we solve Newton's equations of motion for this system until the properties of the system no longer change with time (we equilibrate the system). After equilibration, we perform the actual measurement. In fact, some of the most common

mistakes that can be made when performing a computer experiment are very similar to the mistakes that can be made in real experiments (e.g., the sample is not prepared correctly, the measurement is too short, the system undergoes an irreversible change during the experiment, or we do not measure what we think) [Frenkel and Smit, 1996]. We call molecular dynamics (MD) a computer simulation technique where the time evolution of a set of interacting atoms is followed by integrating their equations of motion. The molecular dynamics can be used to investigate the detailed atomistic mechanisms. With MD technique it is possible to simulate the dynamic, thermal behaviour of atoms in solids. By performing simulations at different temperatures and studying the displacements of the ions as a function of time we can predict diffusion coefficients

The molecular dynamics technique involves solving Newton's laws of motion over a finite time period for all the particles of a system. The main difference with the energy minimization method discussed in the previous section, is that, molecular dynamics simulation gives the effect of temperature by assigning kinetic energy to the atoms in the simulation cell and thus allows us to follow the trajectory of the atoms and molecules with time. Hence, unlike in energy minimization calculations, atoms and molecules can potentially jump over energy barriers to reach a global minimum; however, due to the very short 'real time' accessible to molecular dynamics simulations, this only applies to small energy barriers, i.e., of the order of few $k_B T$. All molecular dynamics simulations in this work were performed using the computer code DL_POLY developed by W. Smith and T.R. Forester in Daresbury, UK.

In molecular dynamics simulation, the particles are initially assigned random velocities, such that the system starts with the required temperature and that the simulation cell has no translational momentum, i.e.,

$$\sum_{i=1}^{N} m_i . v_i^2 = 3Nk_B T \qquad (2.1)$$

and

$$\sum_{i=1}^{N} m_i . v_i = 0 \qquad (2.2)$$

where N is the number of particles, k_B is the Boltzmann constant, T is the temperature, m_i is the mass of ion i_i, and v_i its velocity.

The second step of a molecular dynamics simulation is to calculate the force acting on each particle. Once the forces, F_i, are obtained the accelerations, a_i, can be calculated and the velocities, v_i, and positions F_i, are updated, for an infinitely small time step, according to

$$a_i(t) = \frac{F_i(t)}{m_i} \qquad (2.3)$$

$$v_i(t + \delta t) = v_i(t) + a_i(t).\delta t \qquad (2.4)$$

$$r_i(t + \delta t) = r_i(t) + v_i(t).\delta t \qquad (2.5)$$

These are the Newton's equations of motion and can only be applied strictly for an infinitesimal time step. In practice, computer codes use integration algorithms such as the Verlet algorithm to solve Newton's equations, as explained in the next section. The choice of the time step δt, in these equations is very important. Indeed if δt is too large, the molecular vibrations will occur within the time step, giving rise to large errors. However, if δt is too small, the particles will take too long to move a significant distance. In addition, another factor needs to be considered to choose the time factor. After each step, run time properties such as the potential energy, the

temperature, or the pressure of the system are calculated. Then the process is repeated several thousand or million times to reach the required simulation time. In the first few tens of thousand steps, the particles' velocities are scaled to meet the desired temperature. This period is called the equilibrium period and it allows for the system to come to equilibrium at a given temperature and pressure before data are collected. Then, the simulation is run as long as possible, without scaling the particles' velocities, to obtain converged averages of the properties of interest and reduce statistical noise.

In molecular dynamics we follow the laws of classical mechanics, and most notably Newton's law:

$$\vec{F}_i = m_i \vec{a}_i \qquad (2.6)$$

for each atom i in a system constituted by N atoms. Here, m_i is the atom mass, $\vec{a}_i = \frac{d^2 \vec{r}_i}{dt^2}$ its acceleration, and $\vec{F}_i$ the force acting upon it, due to the interactions with other atoms.

In the next section we discuss the integration algorithm, the different types of ensembles used in this work and we will discuss the properties that are calculated from molecular dynamics simulations i.e Radial distribution functions, diffusion coefficients and mean squared displacement.

Integration Algorithms

An integration algorithm is used to perform the step by step solution of the equations of motion using a finite difference algorithm. The algorithm used is this work is the

Verlet algorithm. The positions, velocities as well as accelerations are obtained by a Taylor expansion of the positions about time t:

$$\begin{aligned} r(t+\delta t) &= r(t) + v(t)\delta t + \frac{1}{2}a(t)\delta t^2 + \frac{1}{6}b(t)\delta t^3 + \ldots \\ v(t+\delta t) &= v(t) + a(t)\delta t + \frac{1}{2}b(t)\delta t^2 + \ldots \\ a(t+\delta t) &= a(t) + b(t)\delta t + \ldots \\ b(t+\delta t) &= b(t) + \ldots \end{aligned} \qquad (2.7)$$

where r is the particle's position, **v** is the velocity, a is the acceleration and b is the third time derivative of r. From Equation (2.7) we can calculate the position of a particle about a position $r(t)$ before and after a time step δt

$$r(t+\delta t) = r(t) + v(t)\delta t + \frac{1}{2}a(t)\delta t^2 + \frac{1}{6}b(t)\delta t^3 + \vartheta(\delta t^4) \qquad (2.8)$$

$$r(t-\delta t) = r(t) - v(t)\delta t + \frac{1}{2}a(t)\delta t^2 - \frac{1}{6}b(t)\delta t^3 + \vartheta(\delta t^4) \qquad (2.9)$$

where $\delta(\delta t^4)$ is the order of accuracy. Now adding (2.8) and (2.9) gives

$$r(t+\delta t) + r(t-\delta t) = 2r(t) + a(t)\delta t^2 + \vartheta(\delta t^4) \qquad (2.10)$$

We notice that Verlet algorithm is time-reversible (i.e. $r(t+\delta t)$ and $r(t-\delta t)$ are interchangeable. Also the absence of velocities, since they are not required but are necessary for the calculation of the kinetic energy. They can be calculated by subtracting Equation (2.9) from (2.8) and obtain:

$$v(t) = \frac{r(t+\delta t) - r(t-\delta t)}{2\delta t} + \vartheta(\delta t^2) \qquad (2.11)$$

Equation (2.10) is accurate to δt^4 while Equation (2.11) is accurate to order δt^2.

Ensembles

Statistical mechanics simulations are performed in different ensembles. The microcanonical or NVE ensemble, its where the number of particles, the volume and energy are the constant quantities. The other ensemble is canonical or NVT ensemble, its where the number of particles, the volume and temperature are the constant quantities. And isothermal-isobaric or NPT ensemble, where the number of particles, pressure and temperature are the constant quantities. Initially a NPT simulation is perfomed on the bulk simulation cell (analogous to a constant pressure simulation in energy minimization) to remove any lattice strains. Thereafter, for example when considering surfaces, constant volume ensembles such as the NVT ensemble are used.

Molecular Dynamics Simulation Properties

The molecular dynamics studies result in various quantities describing the temperature-dependent behaviour of the analyzed systems. In our case we looked at the radial distribution functions (RDFs), mean squared displacement (MSD), and diffusion coefficient. These quantities provide the structural information about the solid and liquid phases and about the melting phenomenon, meaning the temperatures of the solid-liquid transition can be estimated. However as stated by Holender (1990) the interpreted temperatures are not the real melting temperatures of the systems, but rather the temperatures of the mechanical instability of the infinite single crystal.

Radial Distribution Functions (RDFs)

The RDF is defined as the probability of finding an atom at a distance r from another atom compared to a homogeneous distribution (Allen and Tildesley, 1987 and Sayle et al., 2002) and is given by

$$g(r) = \frac{V}{N_1 N_2} \frac{1}{4\pi r^2 \delta r} \left\langle \sum_i \sum_{j>i} \delta(r - r_{ij}) \right\rangle \qquad (2.12)$$

where V is the volume, N_1 and N_2 are the atom types of the RDF. The delta function must give rise to a value of one for a range of $r(\delta r)$. The RDF tends to 1 at long distances with sharp peaks indicating a regular lattice structure. For amorphous or liquid systems the RDF shows characteristically a small number of broad peaks at short distance, indicating short range order, superimposed on an oscillating trace to 1, which indicates a loss of long range order (Allen and Tildesley, 1987 and Sayle et al. 2002). The structural properties of our system were investigated by analysing the partial radial distribution functions (RDFs), $g_{FeS}(r)$, $g_{SS}(r)$. The partial RDFs $g_{\alpha\beta}(r)$ are defined in such a way that, by considering an atom of the species α, the probability of finding an atom of the species β in a spherical shell $(r, r + dr)$ is:

$$\rho_\beta 4\pi r^2 g_{\alpha\beta}(r) dr \qquad (2.13)$$

where $\rho_\beta = {}^{x_\beta}\!/_{V}$, is the number density of the species β with mole fraction x_β, and V is the volume per atom.

RDFs give the probability of finding the centre of a particle or atom at a given distance from the centre of another particle. We calculated the partial distribution functions obtaining the nearest neighbour interatomic distances of Fe-S and S-S.

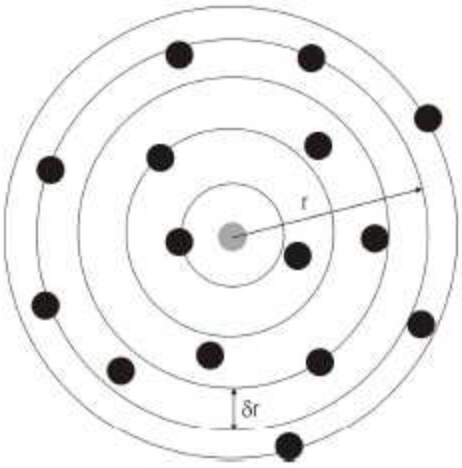

Figure 2.1: Schematic representation of the radial distribution function

The light atom at the center is the reference atom, and the circles around it represent the other atoms. A ring centered on the reference is drawn with radius r and thickness dr. The radial distribution function can be an effective way of describing the structure of a system at different temperatures.

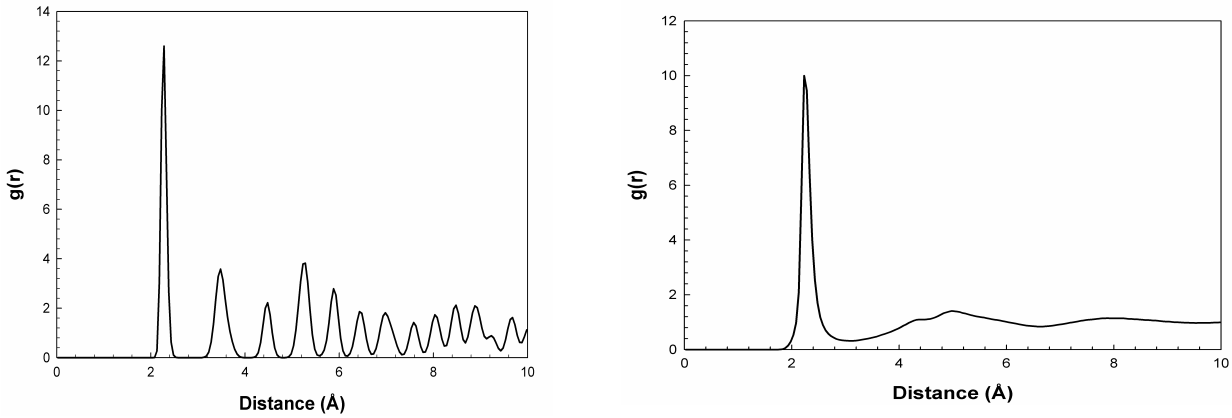

Figure 2.2: Example of an Iron-Sulphur RDF in a crystalline solid on the left and in a liquid phase on the right.

Differentiation between a solid and a liquid can be made using the rdfs by the number of peaks appearing in a particular RDF plot. In a crystal or solid, the radial distribution functions have a multiple number of sharp peaks and heights are characteristic of the lattice structure. The radial distribution function of a liquid has a small number of peaks at short distances and the height of the peaks decreases. The examples of iron-sulphur radial distribution functions are given in Figure 2.2. For the crystalline solid, the peaks are sharp and thin and show long-range order. In case of a liquid phase, the peaks are broad and the radial distribution function rapidly converges to one.

Mean Squared Displacement (MSD)

In this study, the behaviour of the mean squared displacement (MSD) as a function of time is also used to discriminate between a solid and a liquid phase as suggested by Kob, (1999). The time dependence of the average mean squared displacement (MSD) is one of the tools to obtain the information on the atom mobility. It is calculated according to the following relationship:

$$6Dt = <| r_i(t) - r_i(0) |^2 > \qquad (2.14)$$

In a solid (i.e. at a lower temperature), there is no diffusion and the MSD is flat. In a liquid (i.e. at a higher temperature), the particles diffuse randomly and the gradient of the curve is proportional to the diffusion coefficient. The curve takes a parabolic shape at the start, this is due to the short time it takes an atom to feel the effect of the other atoms. If there is no increase in the MSD of an ion type with time, then the ions are vibrating about their mean lattice site. If the MSD's increases with time, then the ions are considered to be moving away from their initial positions (Oliver et al. 1995).

Diffusion Coefficient

The diffusion coefficient is another measure to estimate the relative nobilities of individual pyrite atoms. It is known that diffusion coefficient can be estimated from the slope of MSD plots using the Einstein relation as follows:

$$D = \frac{1}{6}\frac{d}{dt} <| r_i(t) - r_i(0) |> \tag{2.15}$$

or from the integral of the velocity autocorrelation function

$$D = \frac{1}{3}\int_0^\infty < v_i(t).v_i(0) > dt \tag{2.16}$$

The melting point of the simulated system can be located by increasing the temperature of a crystalline system until diffusion appears.

Periodic Boundary Conditions

Periodic boundary conditions are used in most of our simulations of molecular dynamics (and energy minimization). Implementing periodic boundary conditions means that the particles are enclosed in a simulation box, and the box is replicated by an infinite number of images. When a particle leaves the simulation box, one image fills the void, shown in Figure 2.3

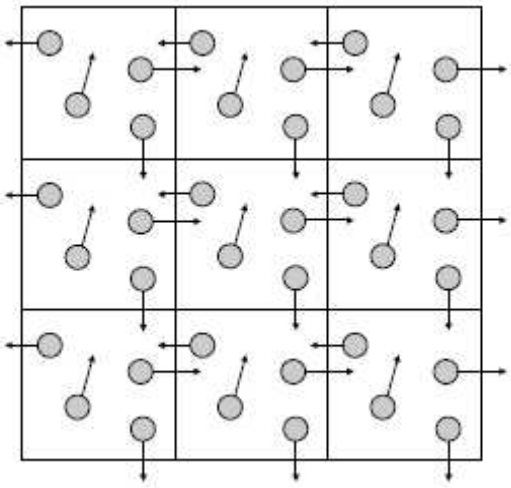

Figure 2.3: Schematic representation of the periodic boundary conditions where the simulation cell is highlighted in bold. Kerisit PhD Thesis (2005)

2.1.3. Surface Energy Calculations

We calculated the surface energy from energy minimization and from molecular dynamics simulations. The surface energy is defined as the excess energy, per unit area of the surface compared to the bulk crystal. Thus any calculation of the surface energy also requires that we model a comparable amount of bulk crystal under identical conditions.

Energy Minimization Surface Energy Calculations

The energy minimization code employed was METADISE. In METADISE calculations, the system is considered to consist of a series of charged planes parallel to the surface and periodic in two dimensions.

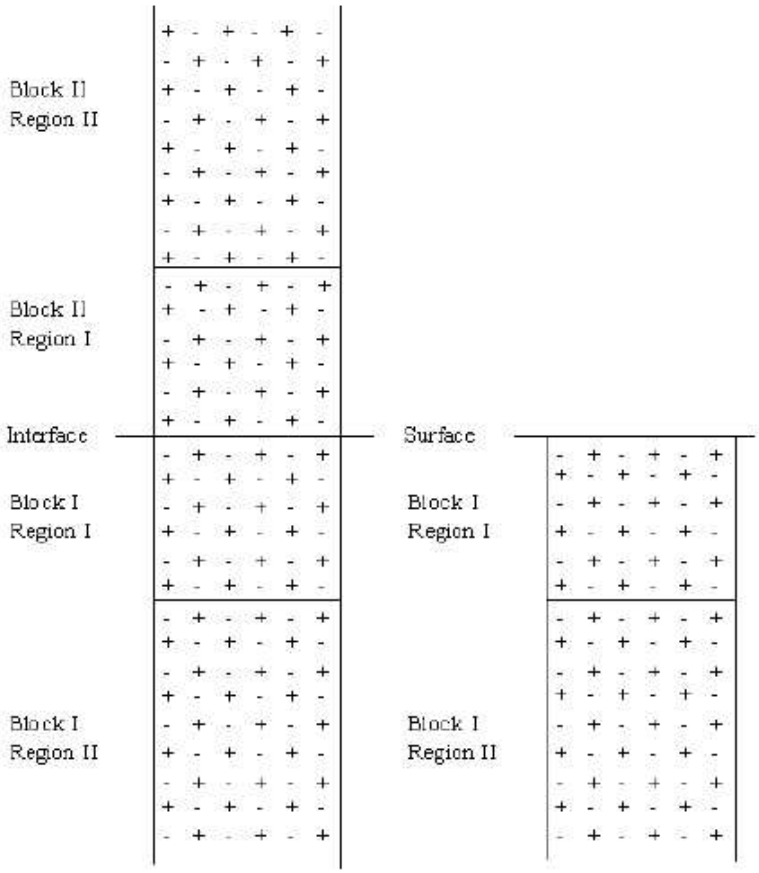

Figure 2.4: The two region approach used in METADISE, the left hand case for a complete crystal unit (BULK) and the right hand case a half crystal exposing a surface. Cooke, PhD Thesis (2003)

A bulk crystal consists of two blocks (see Figure 2.4) and each block has two regions, namely region I and region II. The ions in region I are allowed to relax relative to region II, while the ions in region II are held fixed at their equilibrium position. When the two blocks are separated the surface will be created. Then the Energy of the crystal consists of two parts:

$$E_{total} = E_1 + E_2 \qquad (2.17)$$

where E_1 is the energy of ions in region I and E_2 is the energy of ions in region II.

The surface energy is a measure of the thermodynamic stability of the surface with a low, positive value indicating a stable surface. The equation to obtain the surface energy in J/m^2 is

$$\gamma = \left(\frac{E_s - E_b}{A} \right) * 16.021 \qquad (2.18)$$

where E_s is the energy of the surface block of the crystal E_b is the energy of the equal number of atoms of the bulk crystal and A is the surface area. The energies are in eV and the area in Å^2. And the bulk energy must be calculated for each surface to account for the boundary interaction energy.

The effect of water on the surfaces can also be modelled, and the surface energy of a hydrated surface is

$$\gamma = \frac{E_h - E_b - nE_{H_2O}}{A} * 16.021 \qquad (2.19)$$

where E_h is the energy of the hydrated surface, n the number of water molecules adsorbed on the surface and E_{H_2O} is the energy of a water molecule, i.e., the water self-energy plus the condensation energy.

Molecular Dynamics Surface Energy Calculations

Molecular dynamics simulations yield the average energy per ion of the bulk block and surface slabs. The surface energy in J/m^2 is calculated as:

$$\gamma = \left(\frac{E_s - \frac{n_s}{n_b} E_b}{2A} \right) * 16.021 \qquad (2.20)$$

where n_s is the number of atoms in a surface and n_b is the number of atoms in a bulk . The surface energy with water can be calculated by:

$$\gamma = \left(\frac{E_{s+H_2O} - \left(\frac{n_s}{n_b} E_b + n_{H_2O} E_{H_2O} \right)}{2A} \right) * 16.021 \qquad (2.21)$$

where E_{s+H_2O} is the energy of the slab with water and n_{H_2O} is the number of water molecules and other parameters are the same as those in previous section.

2.2. Types of Surfaces

In this section we discuss types of surfaces that are simulated. Following the classification of Tasker (1979), there are three types of surfaces (see Figure 2.5):

1. Type I surface has a repeat unit cell where all the anions and cations in the same plane are in stoichiometric ratio. Each plane has no net charge meaning there is no dipole moment perpendicular to the surface (example MgO (100)).
2. Type II surface has a stacking sequence of charged planes, but the repeat unit consists of several planes, which when considered together have no dipole moment perpendicular to the surface (example CaF (111)).
3. Type III surface are made up of a stack of alternately charged planes and produce a dipole moment perpendicular to the surface if cut between any planes. In nature these surfaces are stabilized by defects and/or adsorbed species (example CaF (111)).

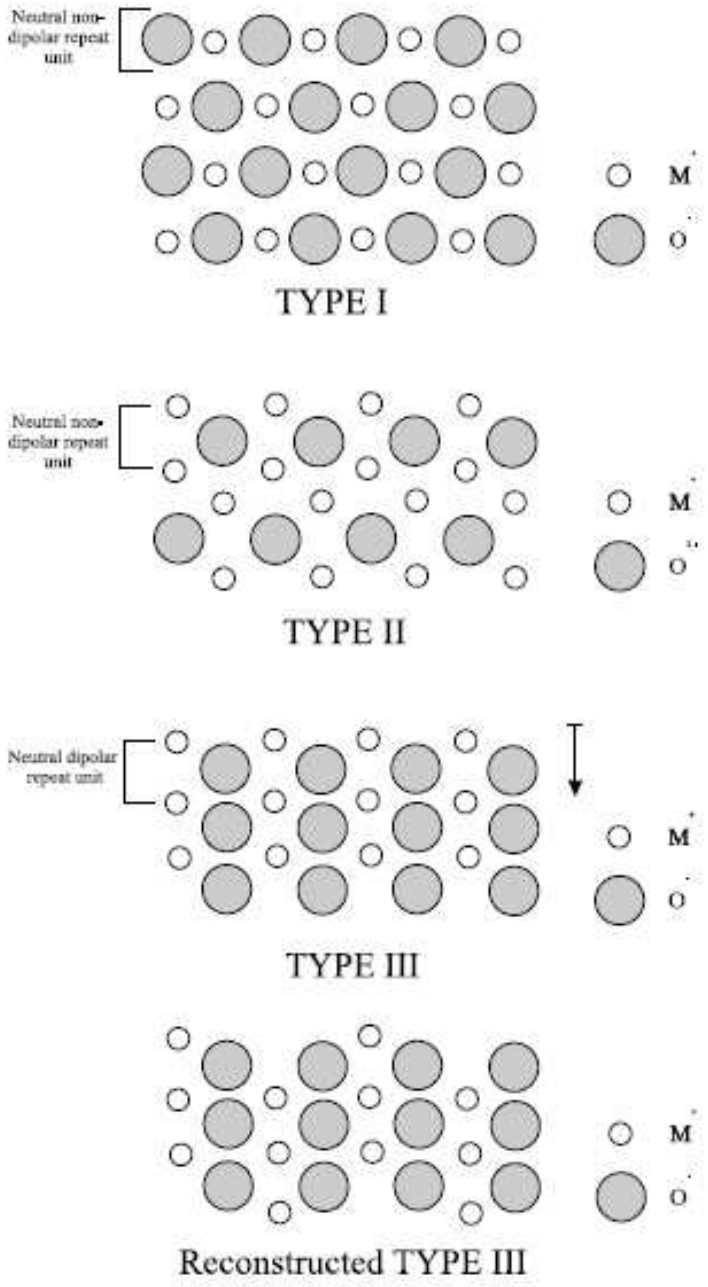

Figure 2.5: Three types of stacking sequences described by Tasker (1979). Picture taken from Kerisit, (2005).

To be able to simulate type III the dipole needs to be removed. One way of doing this is to remove half ions at the top layer and transferring them to the bottom of the unit cell.

Chapter 3

The Potential Model

Potential models describe the variation in the energy of the molecule or solid as a function of atomic coordinates [Catlow, 1997]. The reliability of the calculations depends on the quality and accuracy of the potential model. The potential model; describes the interactions between two or more species. The different Coulombic summation schemes that have been employed are described. Finally, the potential functions used in this study are presented and all the potential parameters are discussed.

3.1. The Born Model of Solids

The atomistic simulation techniques used in this study are based on the Born model of solids [Born and Huang, 1954]. In Born model of solids, it is assumed that the energy and its derivatives can be defined as the summation of all interactions between the atoms in the system which give rise to the total interaction and total net force acting on each atom due to others [Mkhonto, 2005]. In this model, the atoms of a system are represented as point-charge particles that interact via long-range electrostatic forces and short-range interactions. Hence, the interaction energy between two ions is obtained by

$$U_{ij} = \frac{1}{4\pi \in_0} \frac{q_i q_j}{r_{ij}} + \Phi\left(r_{ij}\right) \tag{3.1}$$

where the first term represents the long-range Coulombic interactions, $\in_0$ is the permittivity of vacuum, q_i and q_j are the ionic charges, and r_{ij} is the interatomic

distance. The second term, $\Phi(r_{ij})$, describes the short-range interactions between ions, which include the repulsion between the electron charge clouds and the van der Waals attraction forces.

The interaction energy of a system is the sum of the pairwise interactions between all ions i and j. Where appropriate, many-body terms are also included to take into account, for example, deviations from equilibrium bond angles. Thus, the overall interaction energy of a system can be written in terms of the atomic positions

$$U_i = \sum_{i}^{N} \sum_{\substack{j \\ j \neq i}}^{N} \frac{1}{4\pi \in_0} \frac{q_i q_j}{r_{ij}} + \sum_{i}^{N} \sum_{\substack{j \\ j \neq i}}^{N} \Phi(r_{ij}) + \sum_{i}^{N} \sum_{\substack{j \\ j \neq i}}^{N} \sum_{\substack{k \\ k \neq i \\ k \neq j}}^{N} \Phi_{ijk}(r_{ijk}) \tag{3.2}$$

The first term of the equation (3.2), the Coulombic energy of the system, cannot be obtained by simply summing all the pairwise electrostatic interactions. This is because the contribution of the point-charges to the electrostatic potential decays as 1/r, which causes the Coulombic term to converge very poorly. Therefore, the electrostatic interactions are calculated using summation methods, such as the Ewald sum for example, as described later in this chapter. The other terms of equation 2, the short-range interactions, converge much faster and thus can usually be calculated by a simple summation.

3.1.1. Long Range Interactions

Coulombic Simulation

The electrostatic interactions between charged particles are long-ranged and hence a particle i will interact with all other particles j in the simulation box and also, with

the periodic images of these particles, including those of i . Therefore, the Coulombic contribution, U_i to the interaction energy is

$$U_i = \frac{1}{2}\left(\frac{1}{4\pi \in_0}\right)\sum_n \sum_{i=1}^{N} \sum_{j=1}^{N} \frac{q_i q_j}{\left|r_{ij} + nL\right|} \tag{3.3}$$

where q_i and q_j represent the charges on particles i and j, r_{ij} is the interatomic distance, $\in_0$ is the permittivity of free space, and L is the set of simulation cell vectors reflecting the periodicity of the simulation box. The sum over n is the sum of all the periodic images where n is the ordered triple of integers that define the periodic images, where n is the ordered triple of integers that define the periodic images of the simulation cell. The prime on the first summation indicates that $i = j$ is ignored for $n = 0$. The problem is that the sum in (3.3) is very slow to converge due to the $1/r$ term. Therefore, one needs a quicker and more reliable summation scheme such as Ewald summation.

Ewald Summation

Ewald summation is an excellent technique for calculating electrostatic interactions in periodic systems and is an efficient technique for summing the interaction between an ion and all its infinite periodic images. In the Ewald method, every particle i, of charge q_i, is assumed to be surrounded by a spherically symmetric charge distribution of opposite sign, which exactly cancels q_i and is usually taken to be a Gaussian distribution such as

$$\rho_i(r) = -q_i\left(\frac{\alpha}{\pi}\right)^{3/2}\exp\left(-\alpha r^2\right) \tag{3.4}$$

where the arbitrary parameter α determines the width of the distribution, and r is the position relative to the centre of the distribution. Therefore, only the fraction of q_i that is not screened contributes to the electrostatic potential due to the particle i. At long distances, this fraction rapidly converges to zero and the screened interactions are thus short-ranged. Therefore, the electrostatic interactions between these screened charges can now be calculated by direct summation in real space.

The total contribution of the screened Coulombic interactions, U_i, to the interaction energy is then given by

$$U_i = \frac{1}{2}\left(\frac{1}{4\pi\in_0}\right)\sum_n\sum_{i=1}^{N}\sum_{j=1}^{N}\frac{q_i q_j}{\left|r_{ij}+nL\right|} * erfc\left(\sqrt{\alpha}\left|r_{ij}+nL\right|\right) \tag{3.5}$$

where erfc(x) is the complementary error function

$$erfc(x) = 1 - \frac{2}{\sqrt{\pi}}\int_0^x \exp\left(-t^2\right)dt \tag{3.6}$$

which tends to zero with increasing x. Therefore, if α is large enough, the only term that contributed to the sum in real space is that with $n = 0$.

Parry Summation

The Parry summation, which is a modification of the Ewald method was used in this study, in the simulations of surfaces, which are two dimensional periodic systems. In this method, the crystal is assumed to consist of a series of charged planes of infinite

size rather than an infinite lattice. When summing the electrostatic interactions the vectors are now divided into in-plane vectors and vectors perpendicular to the plane. Hence the reciprocal space term needs to be modified to account for the fact that the overall charge of a plane of atoms can be different from zero.

3.1.2. Short Range Interactions

The short range interactions consist of different contributions. At small distances electron charge clouds will start to interact strongly and therefore will repel each other. Also, at these distances, the dipole-dipole interactions, due to fluctuating dipoles on each ion, will result in attractive van der Waals forces. In addition, when considering covalent systems, the short-range interactions between three or more ions can also be included in the model to represent directionality in the bonding. In this work, the short-range attractive and repulsive interactions are described by simple parameterised potential functions. The potential parameters can be derived empirically by fitting to experimental data, such as crystallographic positions, elastic or dielectric properties, and infrared frequencies, or, by fitting to more accurate simulations such as electronic calculations.

One of the issues that will be addressed in this thesis is that of the transferability of potential parameters. Can potential parameters be employed to model systems that are significantly different from those they have been derived for? In Chapter 5, it will be shown that potential parameters derived to reproduce the interactions between water and nanoparticle.

Lennard-Jones Potential

The Leonard-Jones potential is often used to describe the intermolecular interactions and takes the form

$$U\left(r_{ij}\right)=\frac{A_{ij}}{r_{ij}^{n}}-\frac{B_{ij}}{r_{ij}^{m}} \tag{3.7}$$

where the most common values for n and m are 12 and 6, respectively. The first term represents the repulsion between electronic clouds, which dominates at very short distances. The second term is the attractive part of the potential and models the van der Waals dispersion forces, which dominate at larger distances.

Buckingham Potential

In the Buckingham potential, the repulsive term is replaced by an exponential term and potential takes the form

$$U(r_{ij}) = A_{ij} * \exp^{-r_{ij}/\rho_{ij}} - \frac{C_{ij}}{r_{ij}^{6}} \tag{3.8}$$

Where A_{ij} and ρ_{ij} are parameters that represent the ion size and hardness, respectively. The first term is known as the Born-Mayer potential and the attraction term was later added to form the Buckingham potential. Very often, for the cation-anion interactions, the attractive term is ignored due to the very small contribution of this term to the short-range potential, or, alternatively, the interaction is subsumed into the A and ρ parameters.

Morse Potential

The Morse potential is used to model the interactions between covalently bonded atoms and has the form

$$U(r_{ij}) = A_{ij} * (1 - \exp^{-B_{ij}*(r_{ij}-r_0))})^2 - A_{ij} \tag{3.9}$$

where A_{ij} is the bond dissociation energy, r_0 is the equilibrium bond distance, and B_{ij} is a function of the slope of the potential energy well. The Coulombic interactions between covalently bonded atoms are often partially or totally ignored as the Morse potential already contains the attractive component of the interaction between neighbours.

Three-Body Potential

A further component of the interactions of covalent species is the bond-bending term, which is added to take into account the energy penalty for deviations from the equilibrium value. Hence, this potential describes the directionality of the bonds and has a simple harmonic form:

$$U(\theta_{ijk}) = \frac{1}{2} k_{ijk} (\theta_{ijk} - \theta_0)^2 \qquad (3.10)$$

where k_{ijk} is the three-body force constant and θ_0 is equilibrium angle

3.2. The Potentials Used in This Work

In this section the potential parameters used to model FeS_2 are discussed. The potentials were adjusted, so that they can handle other parameters like elastic constants and most importantly the S-S intramolecular distance well.

Pyrite Potential Parameters

The interatomic potential for pyrite were first derived by [Sithole et al, 2000] they were called HS3 potentials. This model employed the Buckingham potentials for the iron-sulphur and sulphur-sulphur interactions. Three-body and four-body potentials were also included to account for the molecular structure. This model uses the rigid ion. The potential parameters are shown in Table 3.1.

PYRITE			
Ion	Charges (e)		Core-Shell
	Core	Shell	Interactions (eV Å^{-2})
Iron (Fe)	+2.00	-	-
Sulphur (S)	-1.00	-	-
BUCKINGHAM POTENTIALS			
Ion pair (ij)	$A_{ij}(eV)$	$\rho_{ij}(Å)$	$C_{ij}(eVÅ^6)$
Fe-S	94813.903707	0.181250	0.00
S-S	1777.083863	0.330800	97.49150
HARMONIC (SPRING) POTENTIALS			
Ion pair (ij)	$k(eV)$	$r_0(Å)$	
S-S (dimer)	8.44	2.63 (New)	
THREE-BODY POTENTIALS			
Ions	$k(eVrad^{-2})$	$\theta_0(°)$	
S-S-Fe	11.0 (New)	109.503	

Table 3.1: Pyrite potential parameters

Water Potential Parameters

Table 3.2 shows the water potentials used in this work. They were derived by de Leeuw and Parker (1997). This potential model uses the core-shell description for the oxygen atom. These potentials were used successfully to simulate the pyrite surfaces

with the original potentials (de Leeuw, et al 2000). They were also used successfully to model surfaces of other structures, magnesium oxide surfaces (de Leeuw and Parker, 1998a) and calcite, aragonite and vaterite (de Leeuw and parker, 1998b).

WATER			
Ion	Charges (e)		Core-Shell
	Core	Shell	Interactions (eV Å^{-2})
Water Oxygen (Ow)	+1.250	-2.050	209.449602
Water Hydrogen (Hw)	+0.400	-	-

BUCKINGHAM POTENTIALS			
Ion pair (ij)	$A_{ij}(eV)$	$\rho_{ij}(Å)$	$C_{ij}(eVÅ^6)$
Hw-Ow	396.27	0.250	10.0

LENNARD-JONES POTENTIALS		
Ion pair (ij)	$A(eVÅ^{12})$	$B(eVÅ^6)$
Ow-Ow	39344.98	42.15

MORSE POTENTIALS				
Ion pair	$D_{ij}(eV)$	$\alpha_{ij}(eV)$	$r_0(Å)$	Coulombic Substraction (%)
Ow-Hw	6.203713	2.22003	0.92367	50

THREE-BODY POTENTIALS		
Ions	$k(eVrad^{-2})$	$\theta_0(°)$
Hw-Ow-Hw	4.19978	108.693195

Table 3.2: Water potential parameters (de Leeuw and Parker (1997)

Pyrite-Water Interactions

The water and pyrite model interactions were first introduced by de Leeuw et al, in 2000, where iron-water oxygen , sulphur-water oxygen , and sulphur-water hydrogen interactions were modelled by Buckingham potentials. The potentials parameters are shown in Table 3.3.

PYRITE-WATER INTERACTIONS			
BUCKINGHAM POTENTIALS			
Ion pair (ij)	$A_{ij}(eV)$	$\rho_{ij}(\mathring{A})$	$C_{ij}(eV\mathring{A}^6)$
Fe-Ow	483.04	0.30840	0.0
S-Hw	495.38	0.25000	0.0
S-Ow	1421.67	0.3308	64.1040

Table 3.3: Potential Parameters for the pyrite-water interactions.

Chapter 4

Results and Discussions:

Effect of Temperature and Water on the Surface Structure and Stability of Pyrite

Pyrite FeS_2 surfaces have been a subject of study for several years. In this chapter we concentrate on the temperature effect on both the surfaces and bulk structure using molecular dynamics technique and the bulk properties such as the lattice parameter, distances, elastic constants where calculated using energy minimisation technique. The following properties; radial distribution functions (RDFs), diffusion coefficients and mean squared displacements (MSD); will depict changes induced by temperature. The influence of water permeates virtually all areas of biochemical, chemical and physical importance, and is especially evident in phenomena occurring at the interfaces solid surfaces (Henderson, 2002). We will also study the effect of water on the surfaces of pyrite, by comparing the surface energies of pure and hydrated surfaces using both molecular dynamics and energy minimisation methods.

4.1 Bulk FeS_2 (Pyrite)

Before the surface energy can be calculated the properties and energy of the perfect bulk crystal have to be calculated. We used a cell containing 768 ions and the simulation was scaled at 100ps at constant pressure (NPT) and 500ps at constant temperature (NVT). Table 4.1 shows the calculated bulk properties from the adjusted interatomic potentials using the METADISE code. Our calculated structural parameters agree very well with the experimental results of Benbattouche et al.

(1989). Figure 4.1 shows the temperature variation of the bulk lattice parameter used in the slab calculations (or the expansion of the lattice with respect to temperature).

Table 4.1: Comparison of the calculated and experimental structure and elastic properties of pyrite (FeS_2)

Parameter	Calculated	Expt. (Benbattouche et al., 1989)
$a(\AA)$	5.385	5.418
$Vol(\AA^3)$	156.16	159.04
Distances (Å)		
S-S	2.170	2.177
Fe-S	2.250	2.262
Fe-Fe	3.810	3.831
Elastic Constants (GPa)		
C_{11}	370.0	366
C_{12}	50.98	47
C_{44}	98.96	105
Bulk Modulus (GPa)	157.5	155

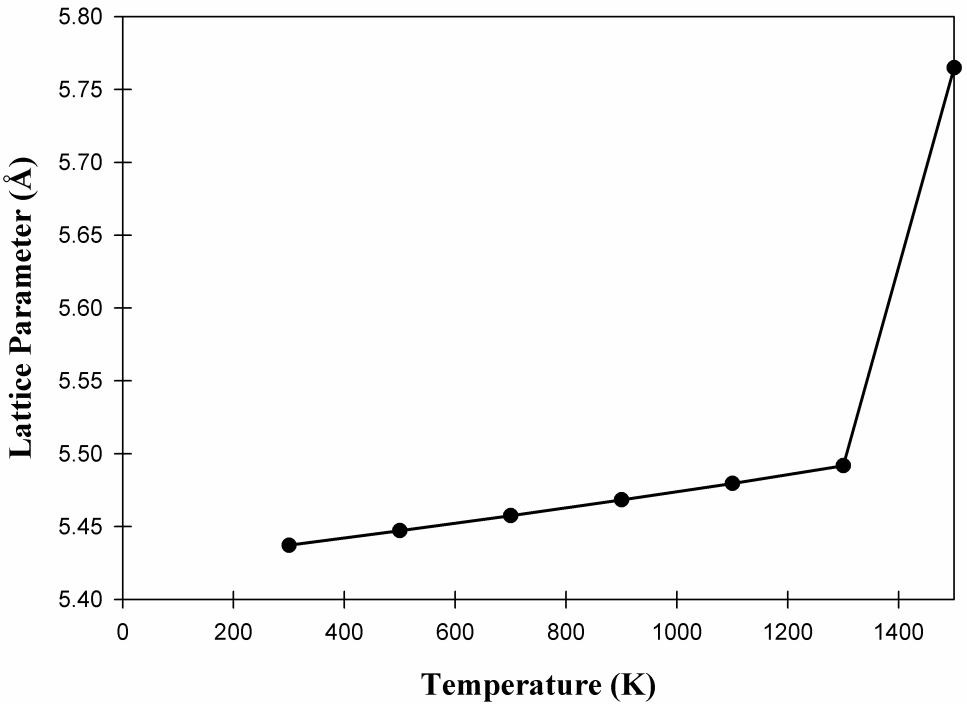

Figure 4.1: Lattice parameter against temperature for FeS_2

The graph shows that the bulk crystal melted between 1300K- 1500K, since the lattice constant increases anomalously in this range. The thermal coefficient of expansion was calculated as 1.45×10^{-6} K^{-1}. Figures 4.2a and b show the bulk structure of FeS_2 simulated at 300K and 1300K, respectively. The structures at 300K and 1300K are clearly not the same. The crystalline structure has completely disappeared at 1300 K and the bulk structure has melted.

From http://www.reade.com/Products/Sulfides/Iron_Sulfide.html the experimental melting point of pyrite is 1466 K. However Sasaki et al. (1999) have mentioned that pyrite has no melting point, but exhibits a peritectic decomposition point at 1016 K where it decomposes to FeS and S. However, we could be able to observe this because as noted earlier our model assumes that the S_2^{2-} does not dissociate. Chen et al (1990) mentioned that the melting of solids is one of the most common observations of a phase transition; the mechanism of melting is still an outstanding problem in condensed matter physics.

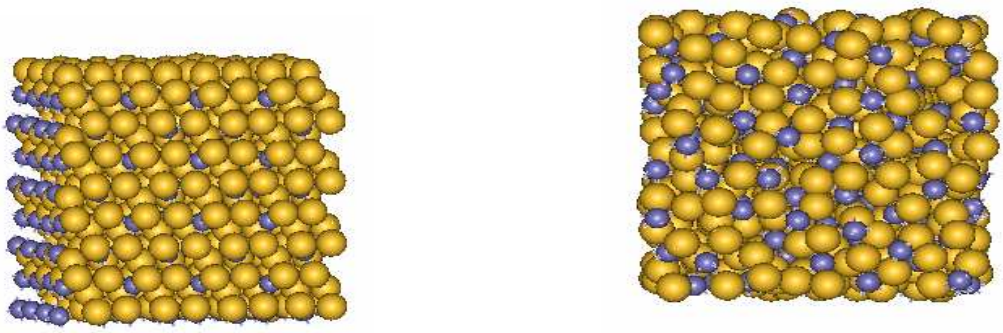

a) **b)**

Figure 4.2: The bulk crystal of FeS_2 at temperatures a) 300 K and b) 1300 K.

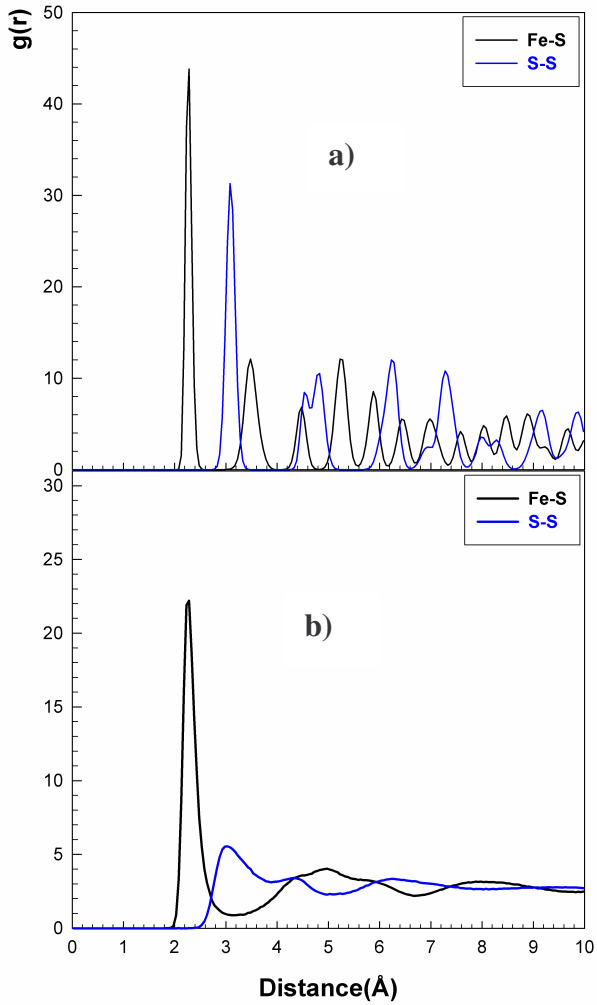

Figure 4.3: The RDFs of FeS_2 bulk structure at: a) 300K and b) 1300K

Figure 4.3 a) shows the RDFs of the bulk pyrite FeS_2 at 300K, which has a well-ordered structure with nearest neighbour distances of 2.28Å and 3.08Å for Fe-S and S-S, respectively. Comparison with the results at 1300 K (Figure 4.3b) shows that the nearest neighbour distances have changed to 2.03Å and 2.58Å for Fe-S and S-S. respectively. Figure 4.3 b) depicts a highly disordered system since the long range order has disappeared – as expected on melting.

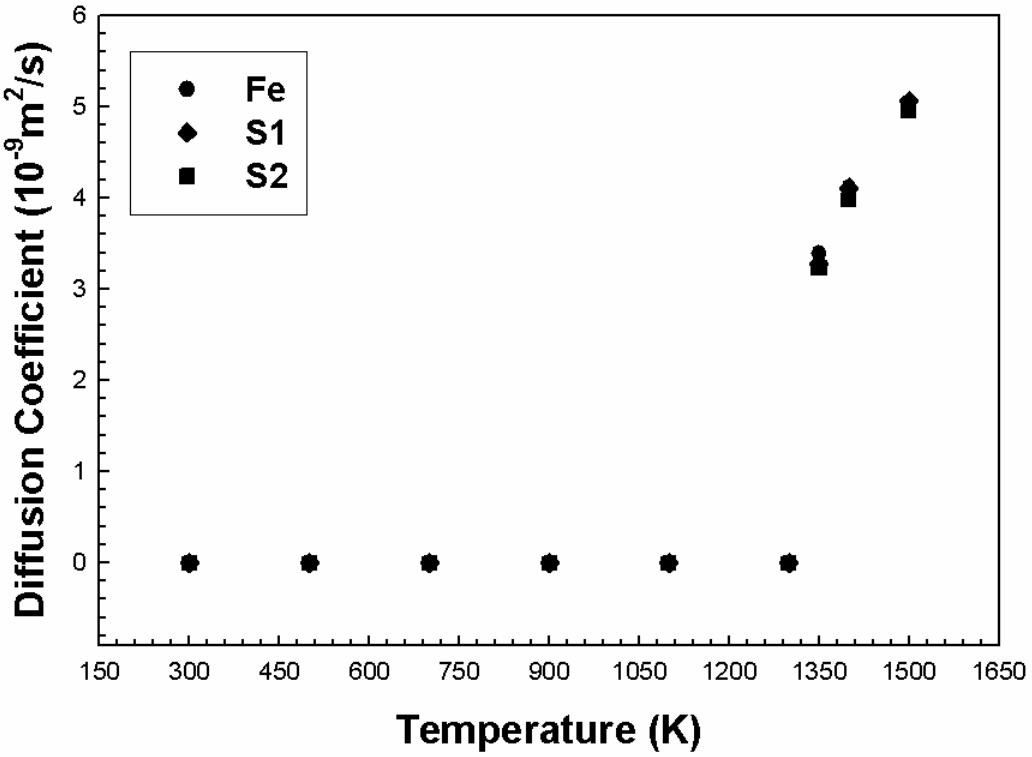

Figure 4.4: Diffusion coefficients of Fe and S ions as function of temperature for bulk structure of pyrite FeS_2.

The melting point of a simulated structure, such as FeS_2 can also be located by increasing the temperature of a crystalline system until ion diffusion appears. In figure 4.4 we have plotted the diffusion coefficients of Fe, S1 and S2 ions as a function of temperature in the bulk structure. These ions start to diffuse at 1350 K, which is the melting point of the bulk structure, which was deduced from the RDFs in Figure 4.3.

4.2 Pure FeS_2 (Pyrite) Surfaces.

Molecular dynamics simulations were performed on the stoichiometric {100}, {110}, {111} and {210} surfaces of FeS_2. We constructed the surfaces by generating slabs, which were periodic and perpendicular to the surface plane in question. The plots of surface energies as a function of temperature, for various S terminated surfaces is given in figure 4.5. The block energy for both surfaces was calculated using a cell of

768 ions and the bulk also contained 768 ions. The simulation conditions were similar to those of the bulk calculations, except that the latter were performe at constant volume.

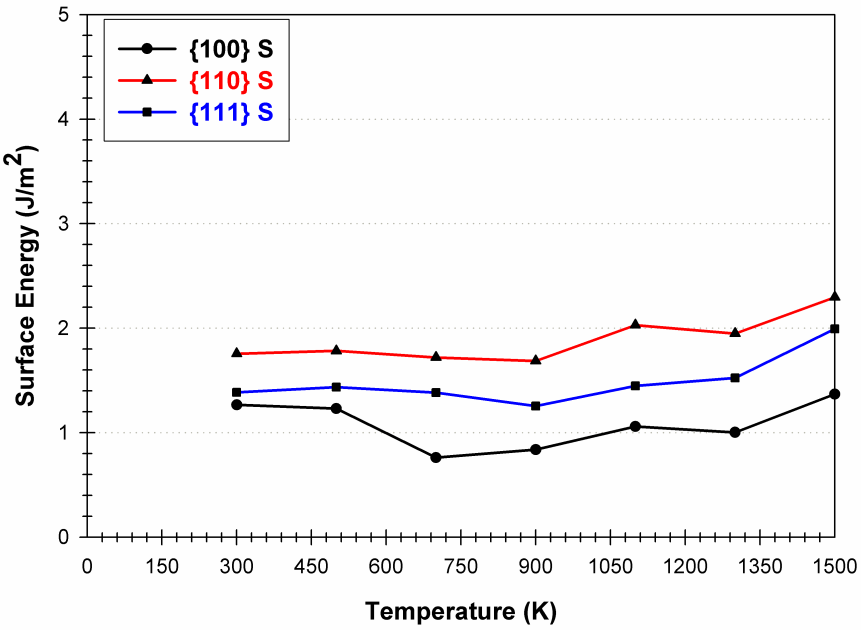

Figure 4.5: Surface energy of pyrite as a function of temperature for the {100} S, {110} S, and {111} S. S denotes that the surface is terminated by sulphur.

Surface energy {100} is the lowest and {110} is the highest, while {111} lies in between.

4.2.1 {100} S Surface

Figure 4.6 (a) and (b) shows the RDFs for the sulphur terminated {100} surface of pyrite at 300 K and at 1100 K, respectively. At 300 K we have a well-ordered structure with many sharp peaks, implying the structure is crystalline. At 1100 K most peaks are not well defined, except for the first peak, which implies surface melting.

Figure 4.7a shows that the {100} sulphur terminated surface of pyrite at 300K has a well-ordered structure, which has a solid phase, the disordered surface at 1100 K is

depicted in figure 4.7b, which has a liquid phase. The surface results obviously show that the molten phase commences at a lower temperature of 1100 K as compared to that of the bulk, which was reported as 1300 K. It is expected, that the melting temperature of bulk is higher than the melting temperature of the surface.

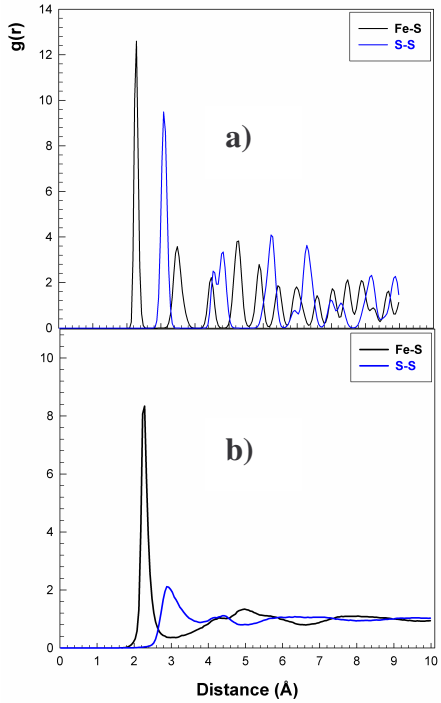

Figure 4.6: The RDFs for (100) S terminated surface of pyrite at a) 300 K and b) 1100 K

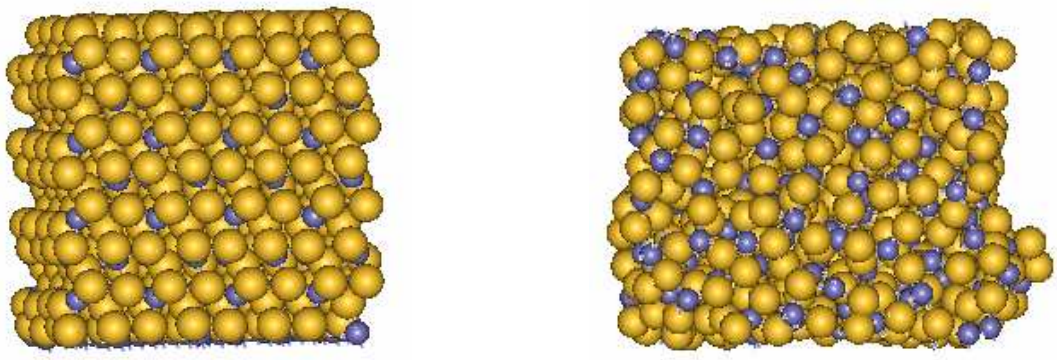

a) **b)**

Figure 4.7: The sulphur terminated structure of pyrite (100) surface at a) 300K and b) 1100K

The time dependence of the average mean squared displacement (MSD) provides useful information on ion mobilities. Figure 4.8 shows that the MSDs of pyrite surface ions with time is constant at 300K which suggests that the diffusion of all ions (Fe, S1, and S2) is negligible. At 900 K the variation of the MSD is noted (Figure 4.9). It can consequently be concluded that ion mobility on the surface has been induced by enhanced temperature.

Figure 4.10 shows the variation of the diffusion coefficients of Fe, S1 and S2 with temperature on the sulphur terminated {100} surface of pyrite. It is quite explicit that a significant increase in the diffusion coefficient occurs between 1100 K and 1500K. After melting ion diffusion tends to a constant value which corresponds to that of a liquid phase. Above 1300 K, the S atoms display a high degree of mobility and diffusivity; which might be ascribed to molecular dynamics simulation being carried out on the {100} S terminated surface.

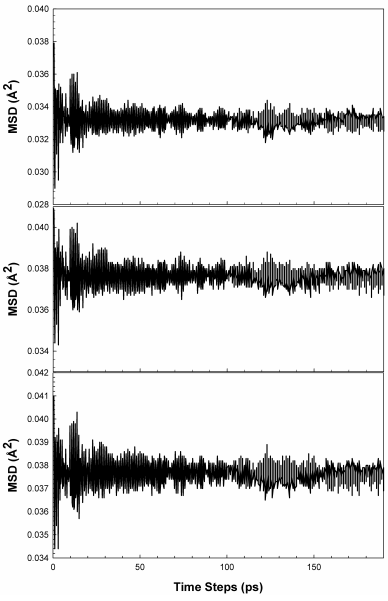

Figure 4.8: Mean squared displacement of {100} S terminated surface of pyrite ions at the temperature of 300 K.

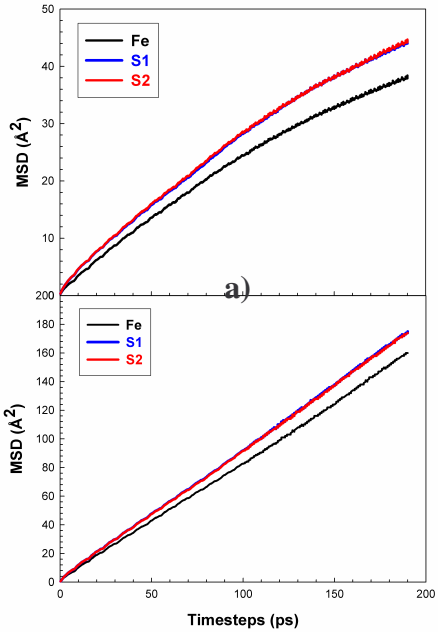

Figure 4.9: Mean squared displacement {100} S terminated surface of pyrite ions at the temperatures of a) 900 K and b) 1100 K

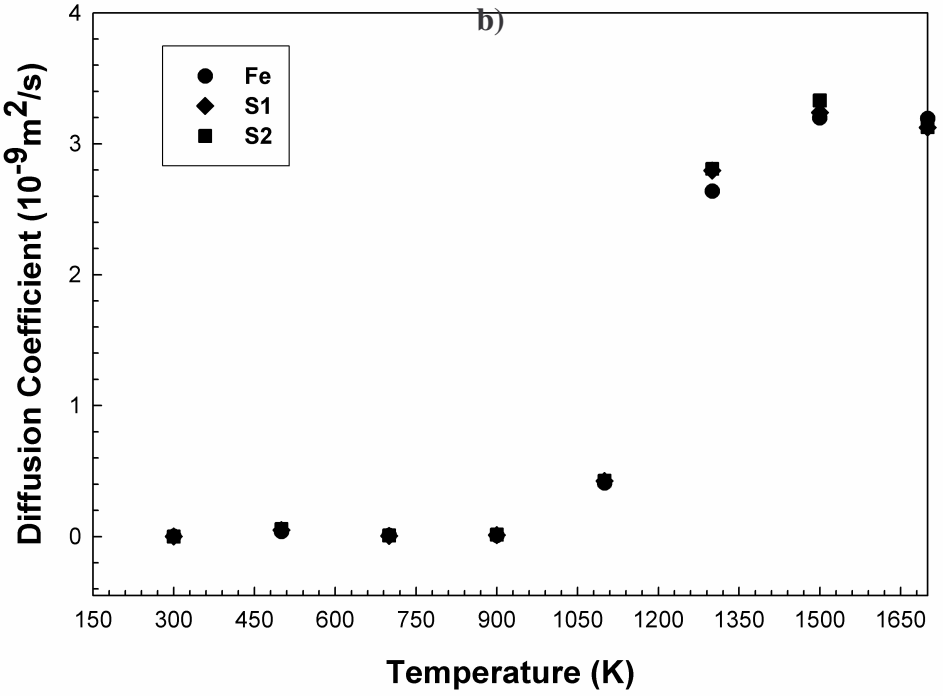

Figure 4.10: Diffusion coefficients of FeS_2 ions as function of temperature for {100} S terminated surface.

4.2.2 {100} Fe Surface

We now consider the {100} surface of pyrite, terminated by iron. Figure 4.11 a)-e) shows five typical mean-square displacement (MSD) against temperature graphs of pyrite at temperatures 300 K, 900 K, 1100 K, 1300 K, and 1500 K respectively. It can be observed that, MSDs of all pyrite ions increase with time from 300 to 1500 K temperatures. At lower temperatures the Fe ion diffuses slowly as compared to the S1 and S2 ions. The slopes of the MSDs versus time of all ions increase with temperature; and it is apparent that diffusion is noticeable at 1100 K. This anomalous enhancement is further demonstrated by the diffusion coefficient vs. temperature graph presented in Figure 4.12; which clearly suggests melting is at 1100 K. The liquid phase of the {100} surface terminated by iron is observed at a temperature of 1100 K, as compared to that of {100} surface terminated by sulphur, which is also at 1100 K. In order to obtain specific information on local structures in FeS_2 the radial distribution functions (RDFs) for all pairs of ions were calculated. Fe-S and S-S RDFs at the temperatures of 300 K, 900 K, 1100 K, 1300 K, and 1500 K are shown in Figure 4.13 (a- e) respectively. At 300 K the surface has a well-ordered structure; and the onset of disorder is noted at 1100 K; which corresponds to the melting point of the {100} surface terminated by sulphur and iron. The liquid phase of the iron terminated surface commences at 1100 K. Figure 4.14 a) and b) shows the well ordered {100} Fe terminated surface at 300 K and the disordered structure at 1100 K respectively. The arrangement of atoms at 1100 K is random as compared to 300 K.

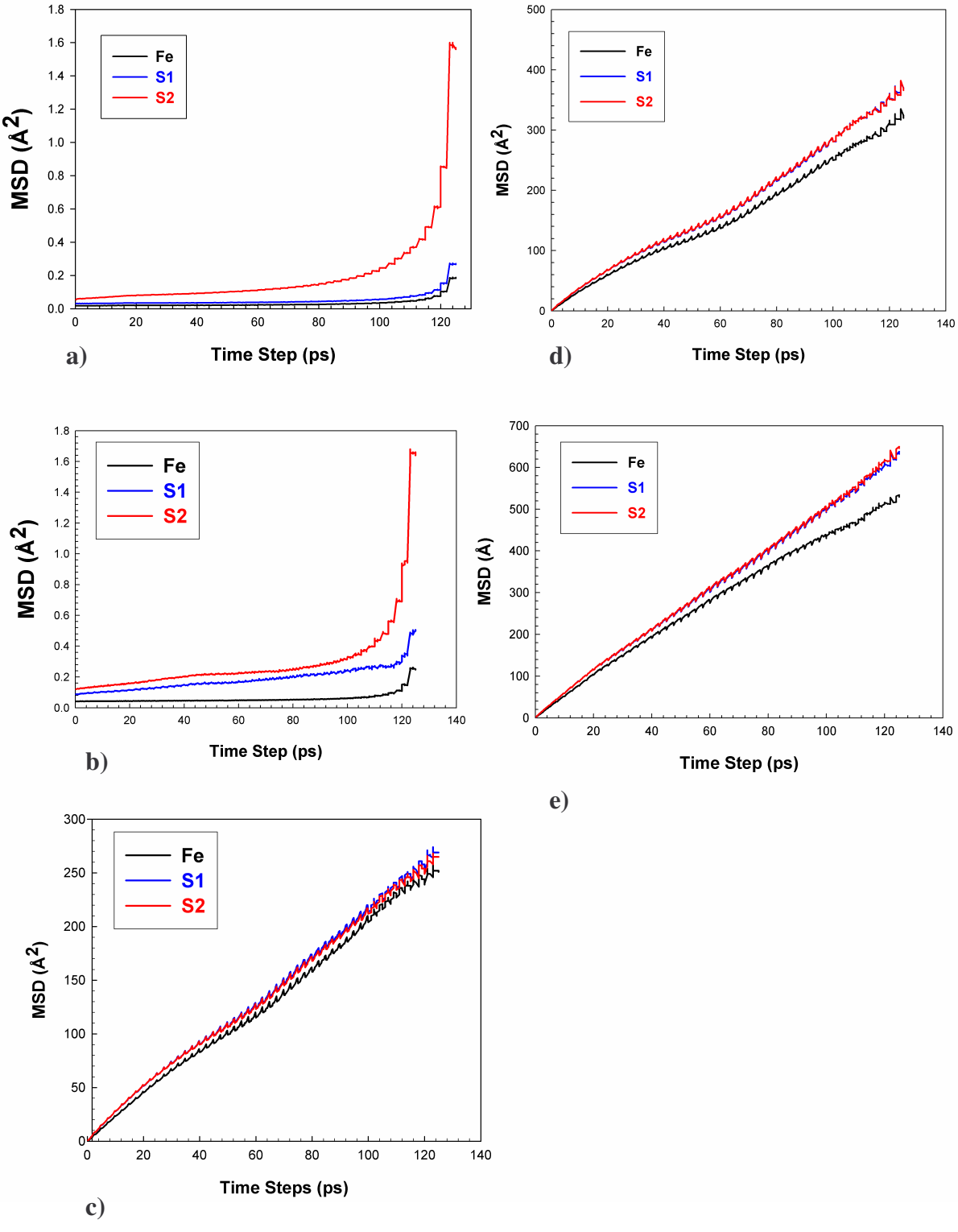

Figure 4.11: Mean square displacement of pyrite ions, i.e. Fe, S1, S2 at the temperatures, a) 300 K b) 900 K, c) 1100 K, d) 1300 K, and e) 1500 K for {100}Fe.

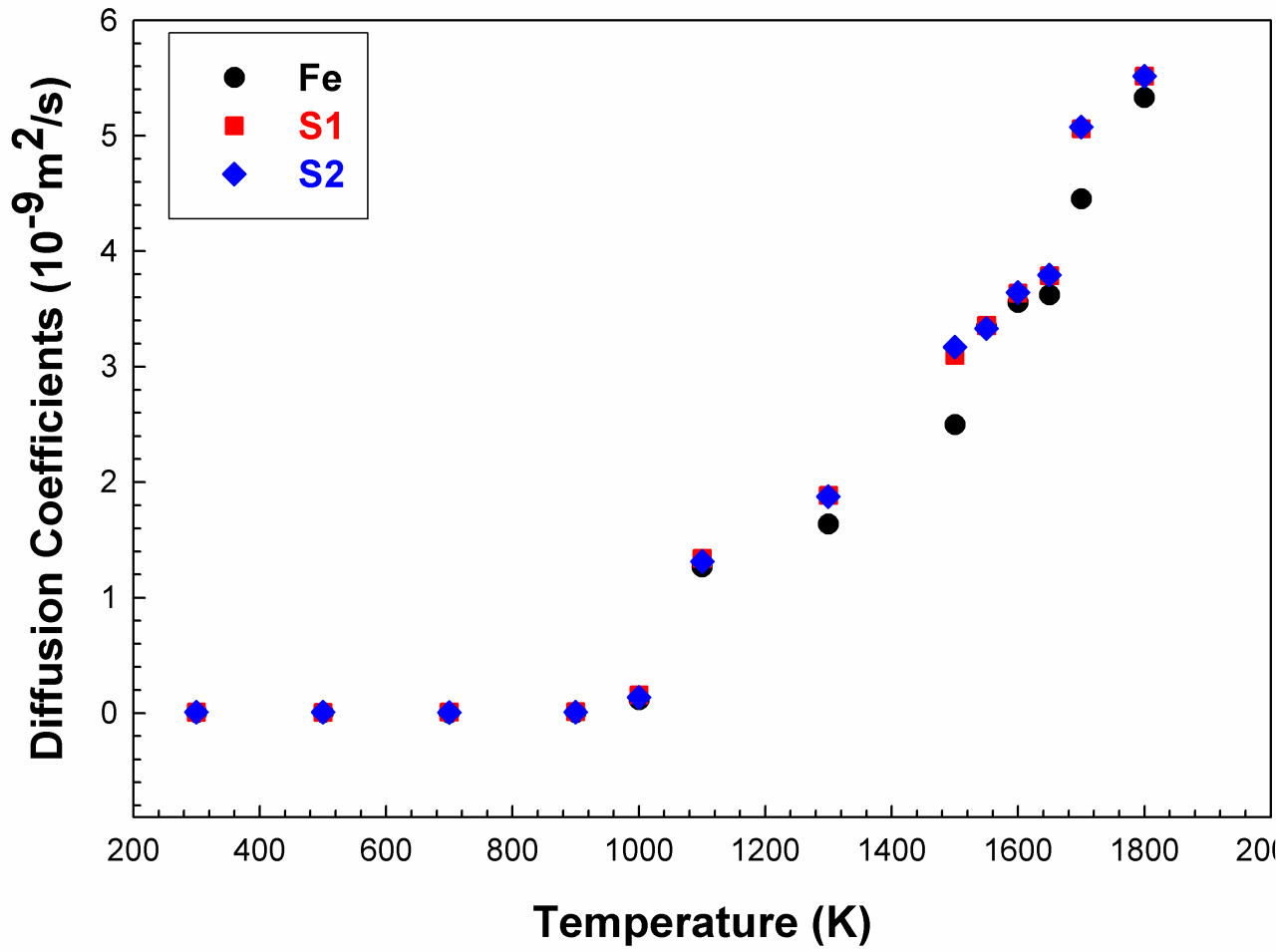

Figure 4.12: Diffusion coefficient as function of temperature for the {100} Fe.

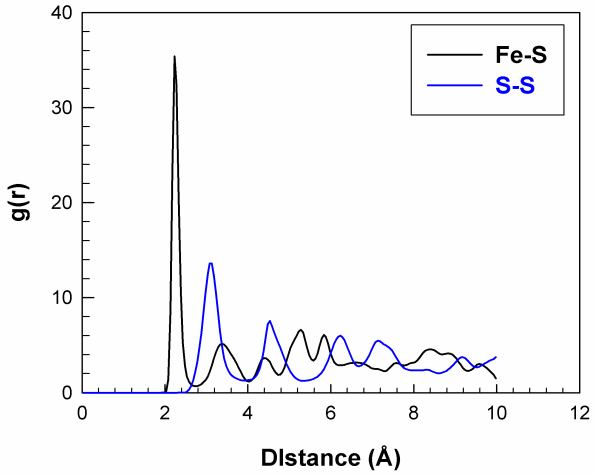

a)

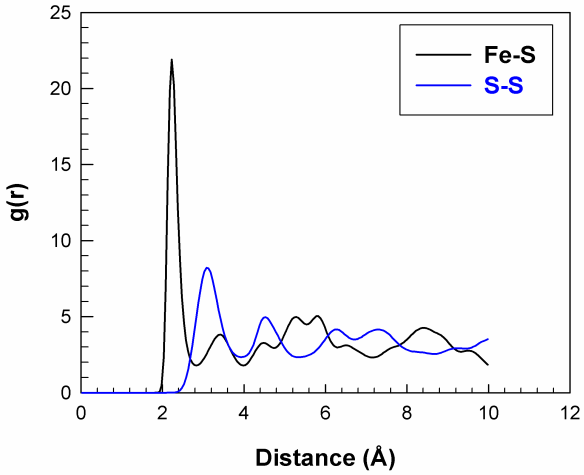

d)

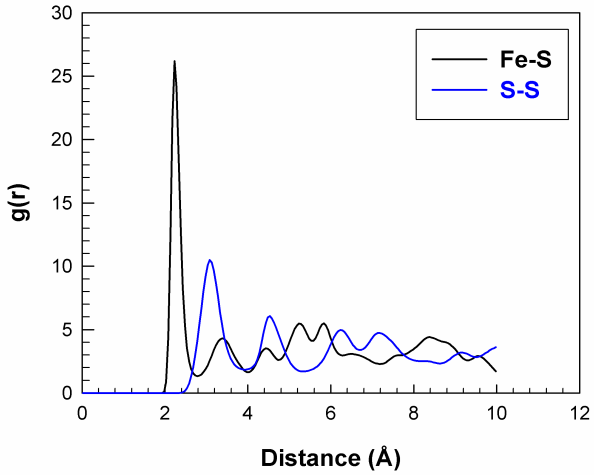

b)

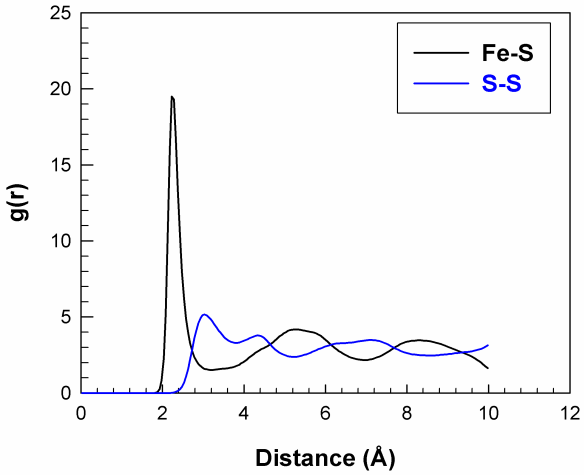

e)

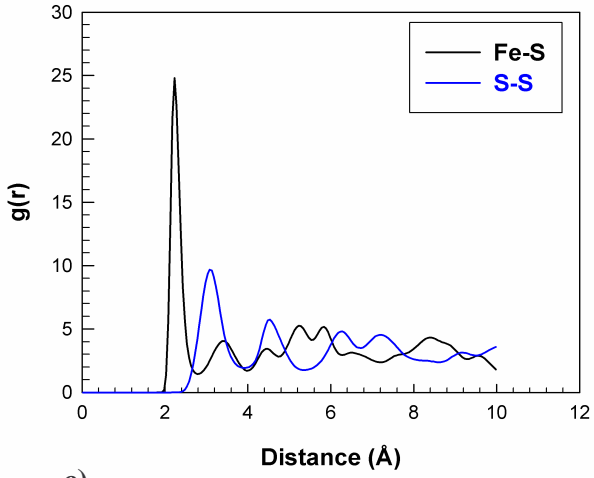

c)

Figure 4.13: The radial distribution functions for pyrite at the temperatures a) 300 K, b) 900 K, c) 1100 K, d) 1300 K, and e) 1500 K for {100} Fe.

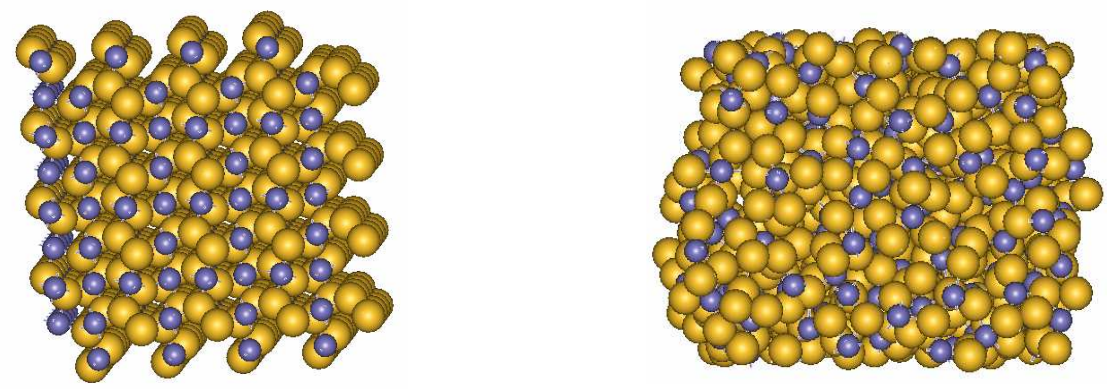

a) b)

Figure 4.14: The structure of the {100} Fe terminated surface at temperatures of a) 300 K and b) 1100 K.

4.2.3 {110} Surface

We now consider the {110} sulphur terminated surface. Figure 4.15 shows the RDFs of the {110} surface at 300 K and 1100 K. The {110} surface has a well-ordered structure at 300 K and we notice the disorder of the surface at 1100 K. The peaks decrease in height and broaden at a high temperatures. The broadening of the peaks at 1100 K is not noticeable, hence in order to justify that 1100 K is our transition temperature, we will study the behaviour of the ion diffusion coefficients of {110} surface.

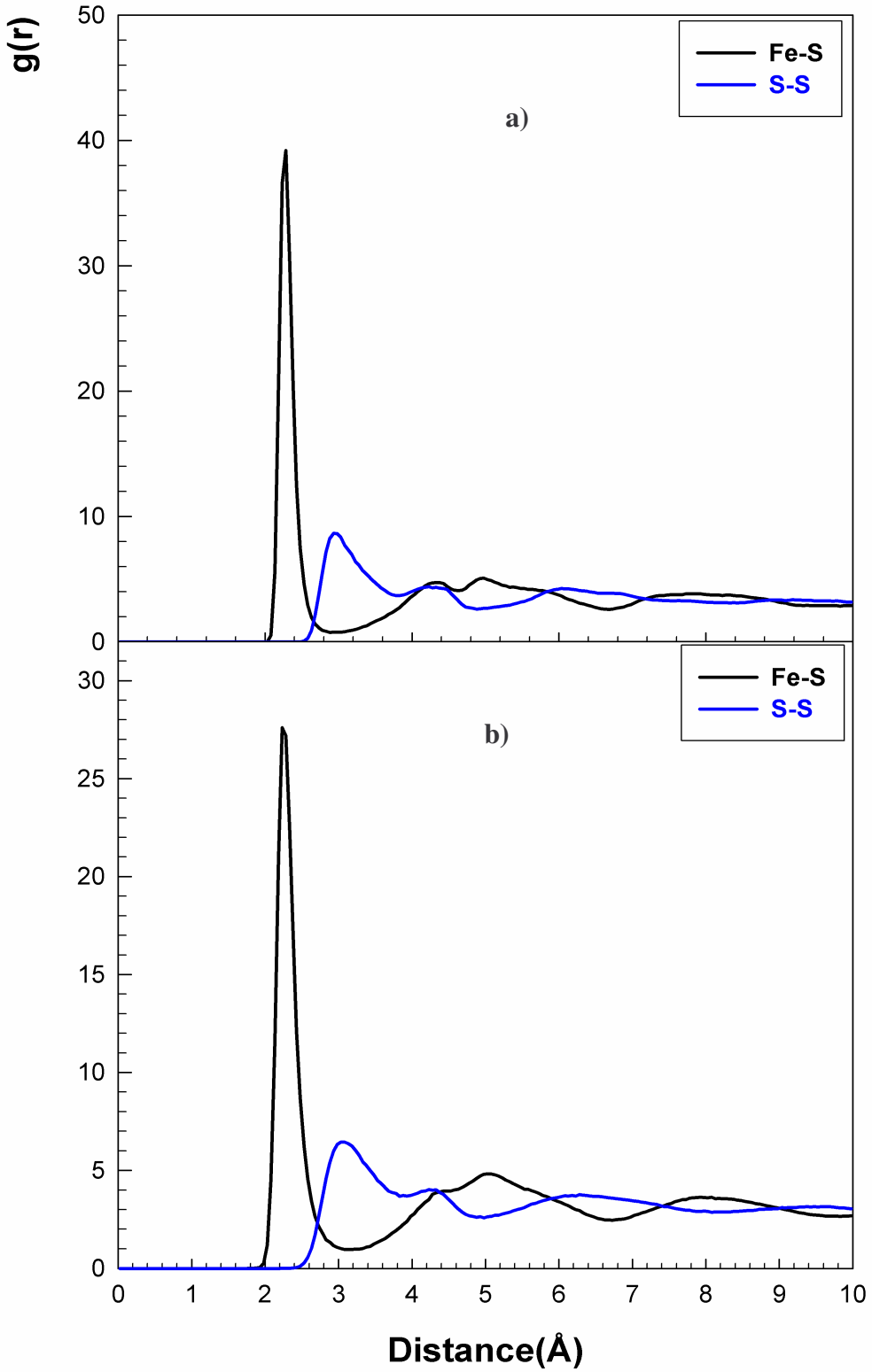

Figure 4.15: The RDFs for {110} surface of pyrite at a) 300 K and b)1100 K

Figure 4.16 shows the increases in the mean squared displacements of pyrite ions as a function of time. This continuous increase of the MSDs for species at each temperature indicates that the system has retained its liquid structure at a temperature of 1100 K. They also indicate that increased temperature induces an increased motion of the mobile phase atoms. It can be observed that, diffusion for pyrite species, increases with an increase in temperature.

Figure 4.17 shows the diffusion coefficient of all ions as a function of temperature; and indeed it increases substantially in the region where melting is expected to occur, i.e. above 1100 K.

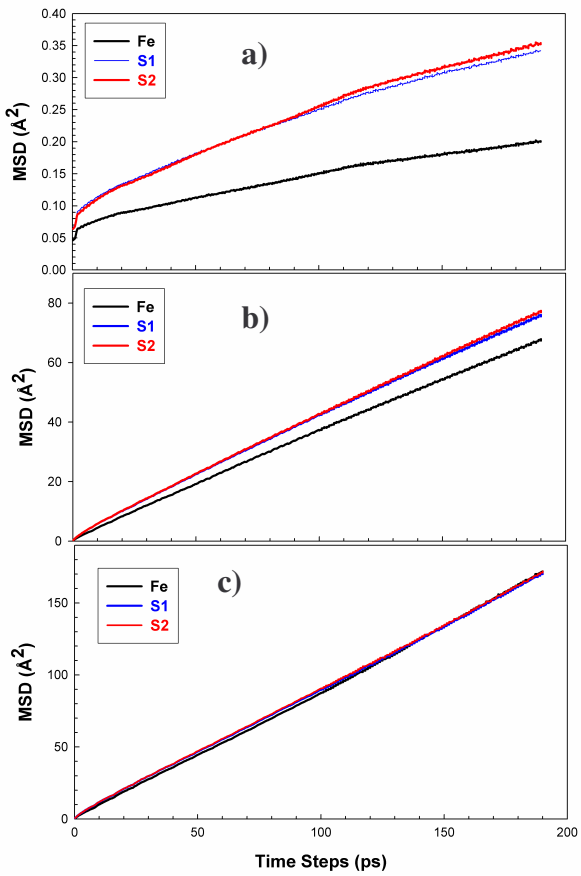

Figure 4.16: Mean squared displacement of pyrite ions for {110} S termination at the temperature of a) 300 K and b) 900 K and c) 1100 K.

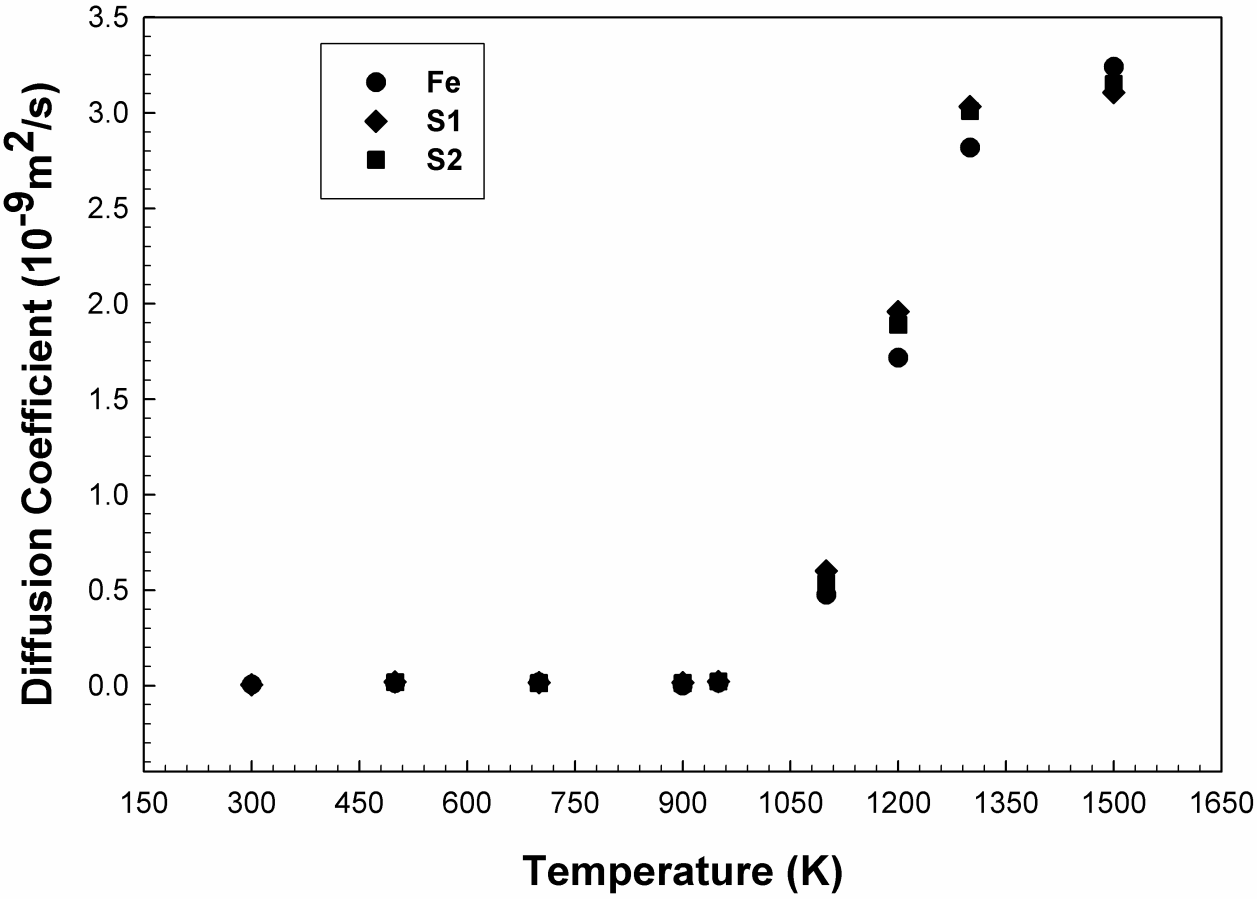

Figure 4.17: Diffusion coefficients of Fe, S1 and S2 as function of temperature for a {110} sulphur terminated surface in pyrite.

a) **b)**

Figure 4.18: The structure of {110} surface at a) 300 K and at b) 1100 K.

Figure 4.18 shows the atomic arrangements of pyrite for the {110} surface at 300 K and 1100 K. It is apparent that the surface has melted at 1100 K, as was observed for the {100} sulphur terminated surface.

4.2.4 {111} Surface

We now consider temperature effects on the {111} sulphur terminated surface. Figure 4.19 shows the RDF of the {111} surface, and it is clear that the structure has a well-ordered structure at 300 K. We notice the disorder of the surface at 1100 K. The peaks decreases in height and broaden at a high temperature. The broadening of the peaks at 1100 K is not noticeable, so to justify that 1100 K is our transition temperature, we will look at the diffusion coefficients on the {111} surface. Figure 4.20 shows the increase of the mean squared displacement of pyrite ions as a function of time. This continuous increase of the MSDs for species at each temperature indicates that the system has attained its liquid structure at a temperature of 1100 K. They also indicate that increased temperature induces an increased motion of the mobile phase atoms. It can be observed that, diffusion for pyrite ions, increases with an increase in temperature.

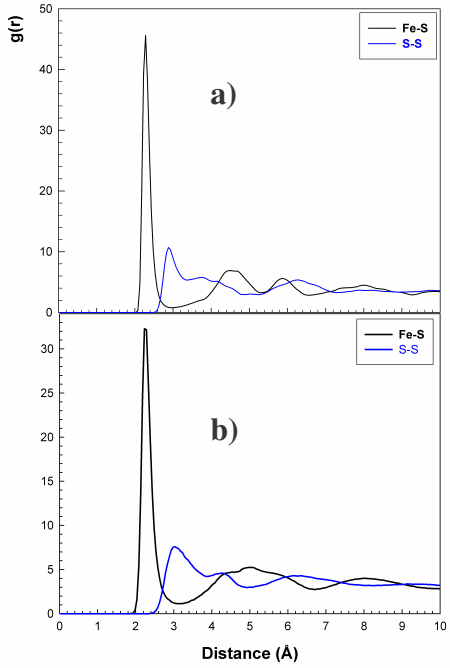

Figure 4.19: The RDFs for {111} surface of pyrite at a) 300 K and b) 1100 K

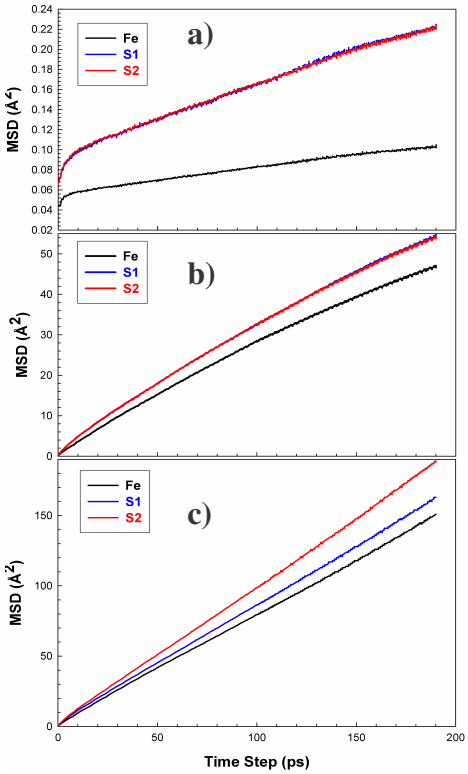

Figure 4.20: Mean squared displacement of pyrite ions at the temperature of a) 300 K and b) 900 K and c) 1100 K.

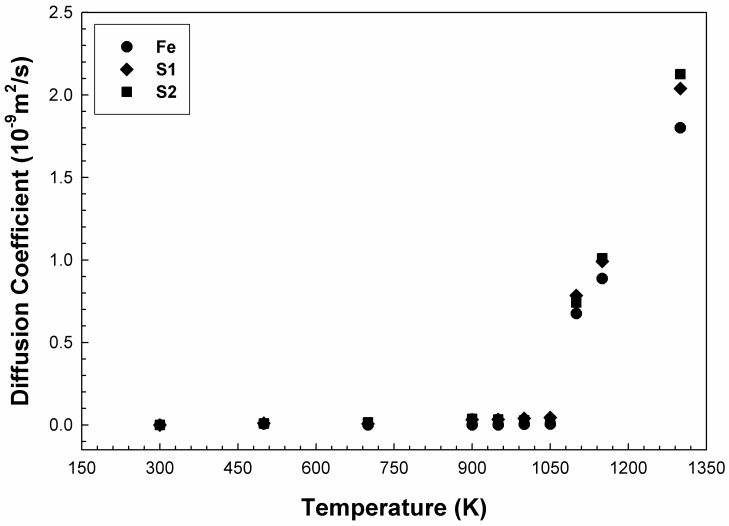

Figure 4.21: Ion diffusion coefficient as function of temperature for the {111} surface of pyrite.

Figure 4.21 shows the diffusion coefficient as a function of temperature. Indeed the diffusion coefficient increase in the region where the phase transition is supposed to occur, at 1100 K. All the Fe, S1 and S2 surface ions start to diffuse rapidly at our observed transition temperature of 1100 K.

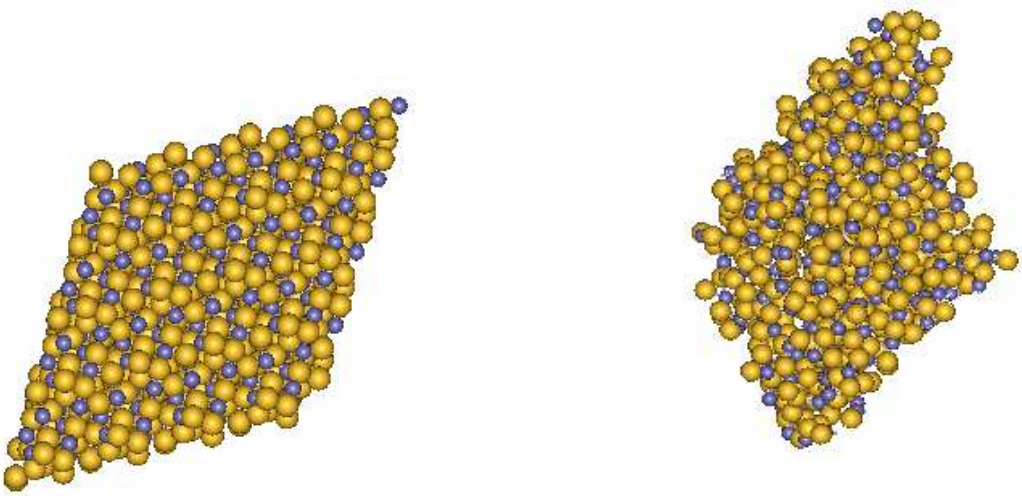

a) b)

Figure 4.22: The structure of {111} surface of pyrite at a) 300 K and b) 1100 K

.

Figure 4.22 shows the structures of {111} surface at 300 K and 1100 K. As in previously studied surfaces {100} and {110}, crystalline structure disappears at 1100K.

4.2.5 {210} Surface

We now consider the {210} surface, terminated by the sulphur. Figure 4.23 shows the RDF of the {210} surface, and it is clear that it has a well-ordered structure at 300 K. We notice the disorder of the surface at 1100 K. The peaks decreases in height and broaden at a high temperature. Similarly to the {111} surface the broadening of the peaks at 1100 K is not noticeable, hence in order to justify that 1100 K is our transition temperature, we consider the diffusion coefficients of the {210} surface. Figure 4.24 shows the increase in the mean squared displacement as a function of time, which increases with time. This continuous increase of the MSDs for species at each temperature indicates that the system has attained its liquid structure at a temperature of 1100 K. They also indicate that increased temperature induces an increased motion of the mobile phase atoms. It can be observed that, diffusion for pyrite species, increases with an increase in temperature.

Figure 4.25 shows the diffusion coefficient of pyrite ions as a function of temperature. Indeed the diffusion coefficient increases in the region where the phase transition is supposed to occur, at 1100 K. Both, the Fe, S1 and S2 surface ions start to diffuse rapidly at our observed transition temperature of 1100 K. Figure 4.26 shows the structures of {210} surface at temperatures of 300 K and 1100 K. It is clear that, the structure loses order at a temperature of 1100 K. Just like the {100}, {110} and {111} surfaces, these results show the formation of the molten phase at 1100 K.

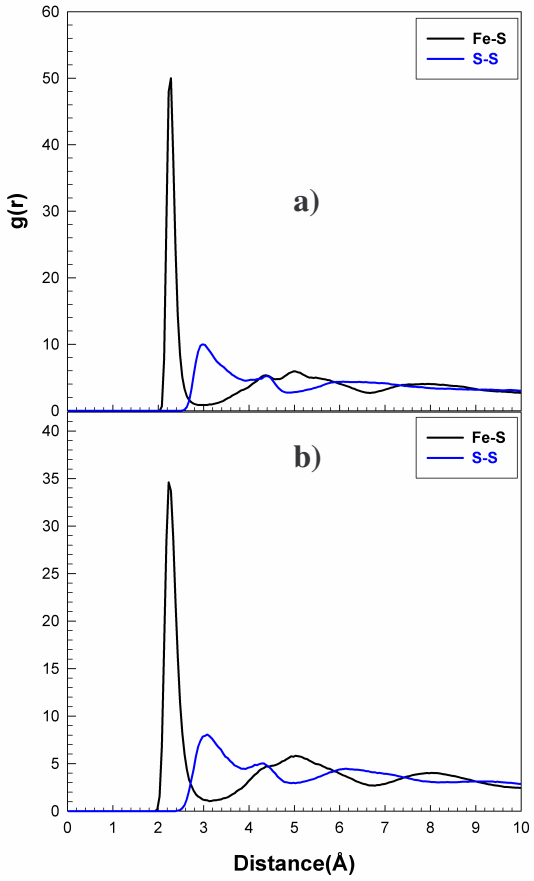

Figure 4.23: The RDFs for {210} surface of pyrite at a) 300 K and b) 1100 K .

.

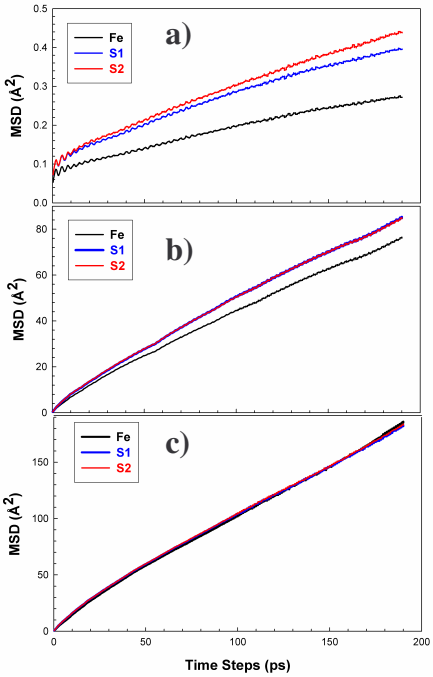

Figure 4.24: Mean squared displacement of pyrite ions at the temperature of a) 300 K and b) 900 K and c) 1100 K

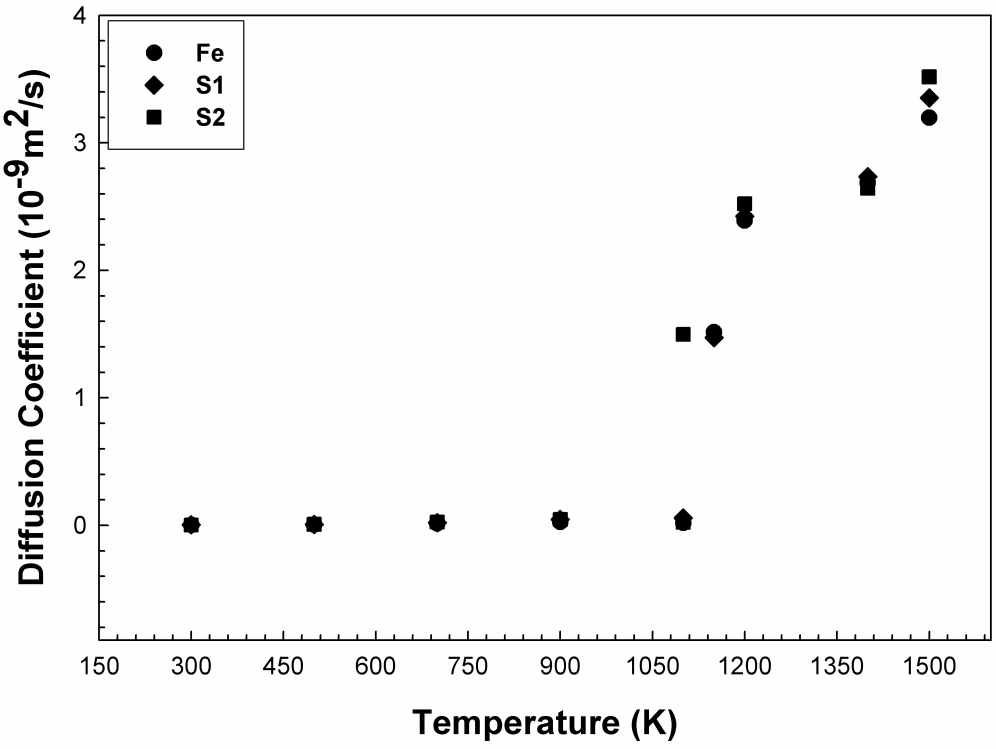

Figure 4.25: Diffusion coefficient of pyrite ions as function of temperature for the {210} S terminated surface

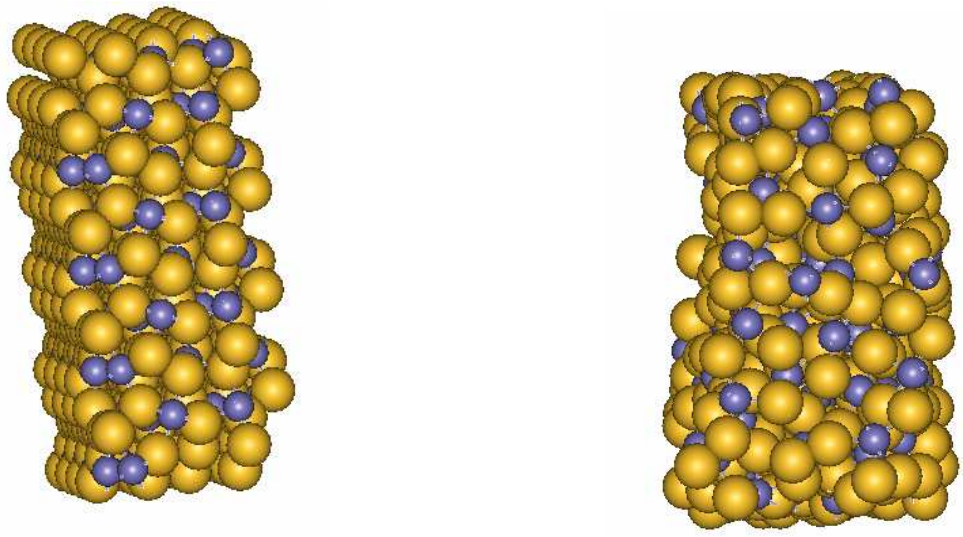

a) **b)**

Figure 4.26: The structures of {210} surface of pyrite at a) 300 K and b) 1100 K

4.3 Surface Energy

In this section we will consider the calculated surface energies of pyrite using both energy minimisation code METADISE and molecular dynamics code DL_POLY. We will also study the hydrated surfaces. Table 4.2 gives the calculated surface energies using energy minimisation method and the calculated surface energies using DFT by Hung et al. (2002a and b). The surface energies for {100}S, {110}S and {210}S compare very well whereas, and our calculated {111} surface energy is very high as compared to their calculated surface energy. The {111} surface is the most unstable S terminated surface of pyrite.

Table 4.2: Calculated surface energies of pyrite using energy minimisation compared with surface energies using DFT by Hung et al. (2002)

Surface	Energy minimization (J/m^{-2})	DFT (Hung et al. 2002a, b) (J/m^{-2})
{100} S	1.04	1.06
{110} S	1.68	1.68
{111} S	3.38	1.40
{210} S	1.66	1.50

De Leeuw et al. (2000) calculated the surface energies of pyrite using the original interatomic potentials and with the unstable surface {111} they got 3.92 J/m^{-2}. This is high as compared to our calculated surface energy. For the stable surface {100} we obtained 1.04 J/m^{-2} with the modified potentials whereas de Leeuw et al (2000) got 1.23 J/m^{-2}. Hung et al (2002a) obtained 1.06 J/m^{-2} which is in good agreement with

our results The {100} surface is more stable when using the modified potentials, implying that they have improved on the stability of the {100} surface.

Now, we consider the surface energies calculated by the MD technique as shown in Table 4.3. Generally, all surface energies are higher as compared to those obtained by energy minimization, except the {111} surface. The higher surface energies from our calculation can be ascribed to temperature effects.

Table 4.3: Calculated surface energies of pyrite using MD technique. Both Surfaces are terminated by S (Sulphur).

Surface	MD (300K) (J/m^{-2})
{100} S	1.26
{110} S	1.76
{111} S	1.19
{210} S	2.04

4.4 Hydrated Surfaces

We next investigated the adsorption of water on pyrite surfaces using the energy minimisation code METADISE. Figure 4.27 shows the structure of the hydrated {100} and {110} surfaces. The addition of water to the surface is initiated by positioning the water oxygen directly above the iron.

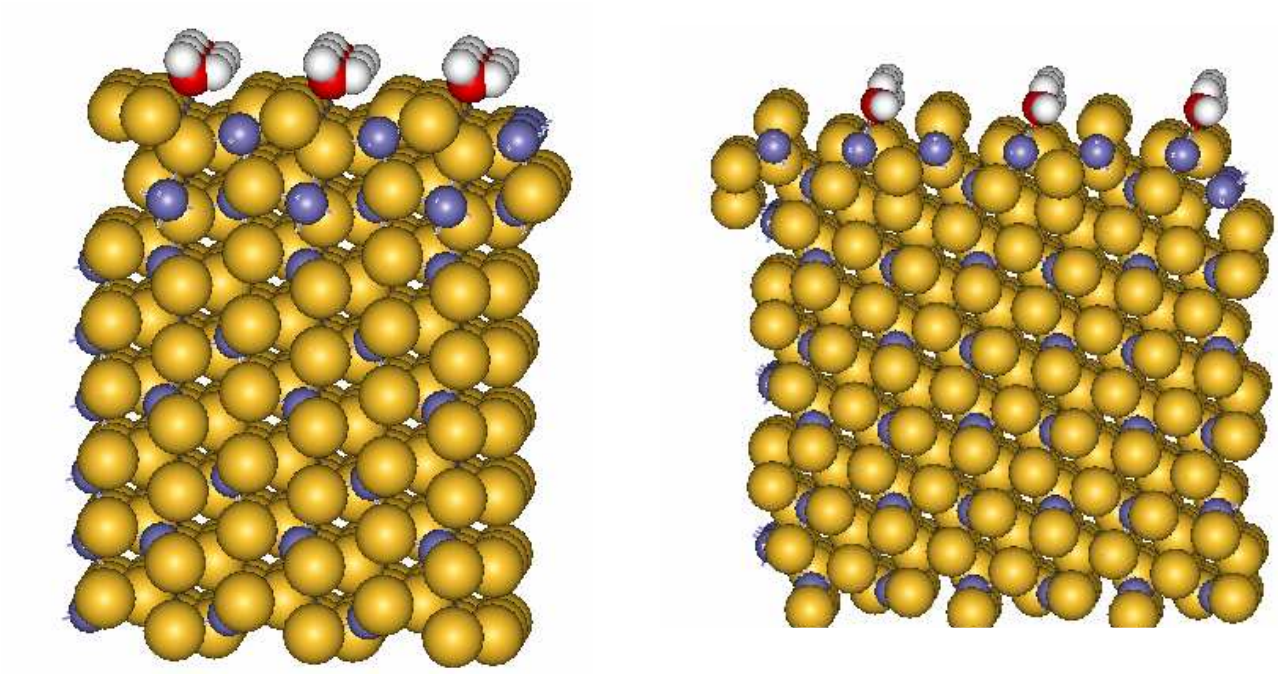

a) **b)**

Figure 4.27: The structure of the hydrated a) {100} and b) {110} pyrite surfaces

Table 4.4: Calculated hydrated surface energies of pyrite.

Surface	Hydrated surface energies (J/m^{-2})
{100} S	0.96
{110} S	1.06
{111} S	2.91
{210} S	1.49

Table 4.4 shows the hydrated surface energies of low index surfaces of pyrite. A comparison with the dry surfaces (Table 4.2) clearly depicts that hydration lowers surface energies, consequently the surfaces are more stable when hydrated. De Leeuw and Parker (1998) have also found that hydration of the surfaces has a stabilizing effect on the following minerals: calcite, aragonite and vaterite. Furthemore, de Leeuw et al. (2000) studied the effect of water on the surface structure and stability of forsterite which confirms this supposition.

4.5 Bulk FeS_2 (Marcasite)

We now study the bulk structure of the pyrite polymorph, marcasite, using our modified potentials; which is a test for the transferability of the potentials. The simulations were executed similarly to those of pyrite, however, the marcasite cell contained 384 ions. Table 4.5 shows the bulk properties of marcasite predicted with energy minimization methods, which agree well with the experimental values. Figures 4.28 a) and b) show the mean-square displacement (MSD) as function of time of marcasite for the temperatures of 300 K and 900 K. At 300 K, there is no sign of ions diffusing; even the values of MSD are very small; the observed fluctuations are probably associated with noise. The MSDs at 300 K and 900 K are almost constant; suggesting negligible mobility. However, the mobility of all ions is noticeable at 1100 K (Figure 4.29). This continuous increase of the MSD with time at 1100 K suggests that marcasite FeS_2 has melted. This is confirmed by the diffusion coefficient vs. temperature curve, in Figure 4.30, where an abrupt enhancement of diffusion of Fe, S1 and S2 is noted above 1050 K.

Table 4.5: Calculated bulk properties of FeS_2 (Marcasite).

Parameter	Calculated	Expt (Kjekshus and Rakke, 1975)
$a(\AA)$	4.402	4.436
$b(\AA)$	5.506	5.414
$c(\AA)$	3.656	3.381
c/a	0.831	0.762
$Vol(\AA^3)$		
Distances (Å)		
S-S	2.25	2.213
Fe-S	2.23	2.230
Fe-Fe	3.60	3.831
Elastic Constants (GPa)		
C_{11}	379.3	
C_{12}	34.1	
C_{13}	103.8	
C_{22}	274.8	
C_{23}	95.7	
C_{33}	414.3	
C_{44}	121.2	
C_{55}	191.3	
C_{66}	146.5	
Bulk Modulus (GPa)	140.6	

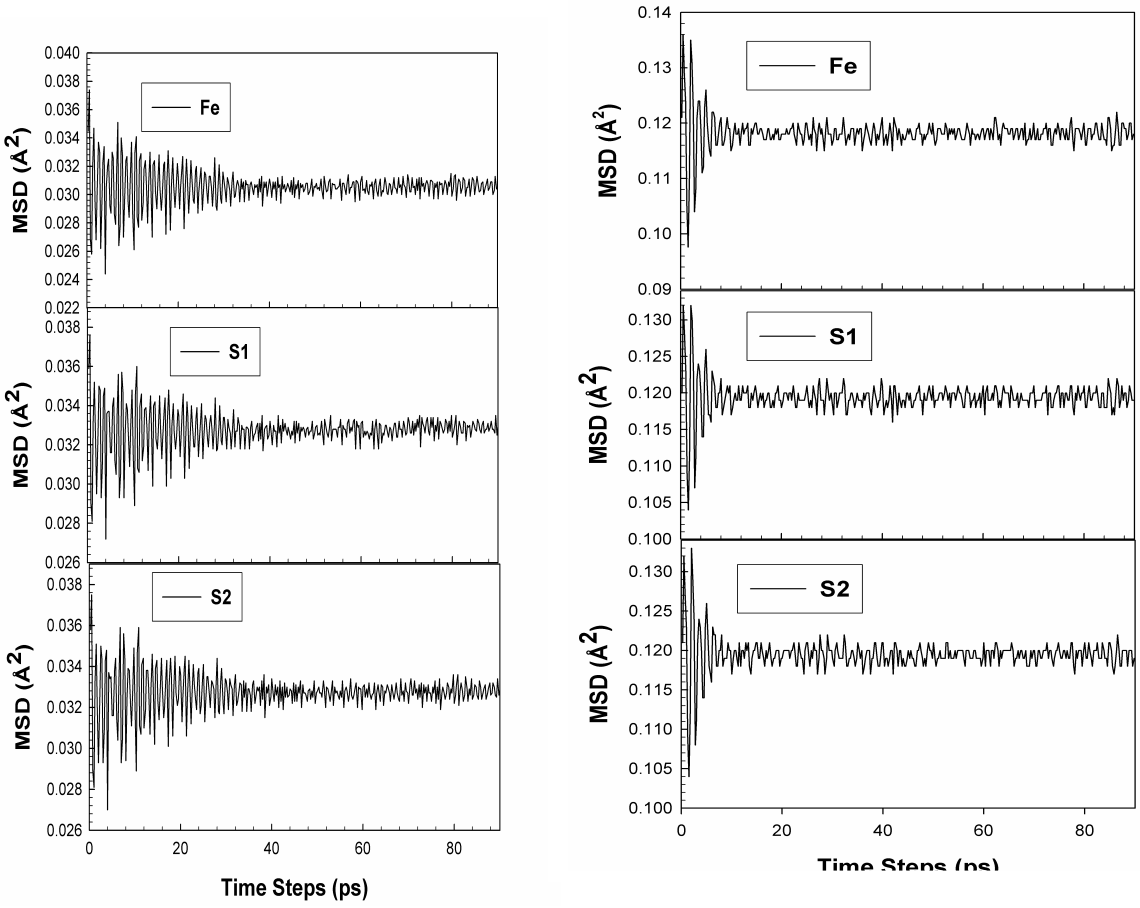

Figure 4.28: The variation of mean squared displacement of all the ions, Fe, S1 and S2 with time at the temperatures of a) 300 K and b) 900 K for marcasite

In order to obtain detailed information on local structures in marcasite FeS_2 the radial distribution functions (RDFs) for all pairs of ions were calculated. Fe-S and S-S RDFs at the temperatures of 300 K, 900 K and 1100 K are shown in Figure 4.31(a-c). At 300 K the bulk has the well-ordered structure and the RDFs have many well defined peaks for both interactions. At 900 K we notice the reduced number of peaks however; there is no sign of bulk melting. The melting of the bulk appears to commence at 1100 K.

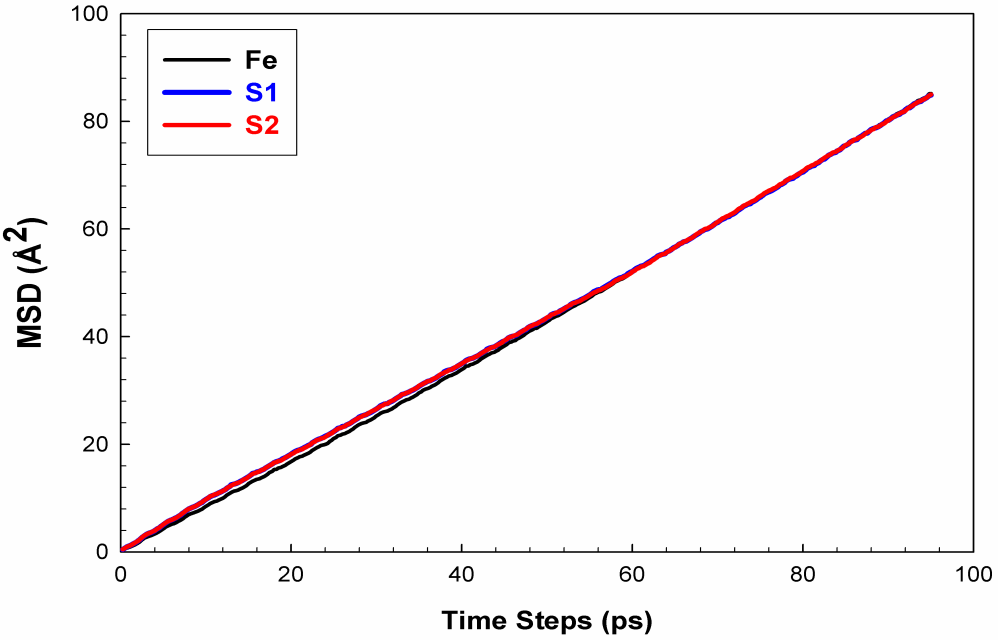

Figure 4.29: The variation of mean squared displacements of the ions, Fe, S1, S2 with time at the temperature 1100 K , for marcasite.

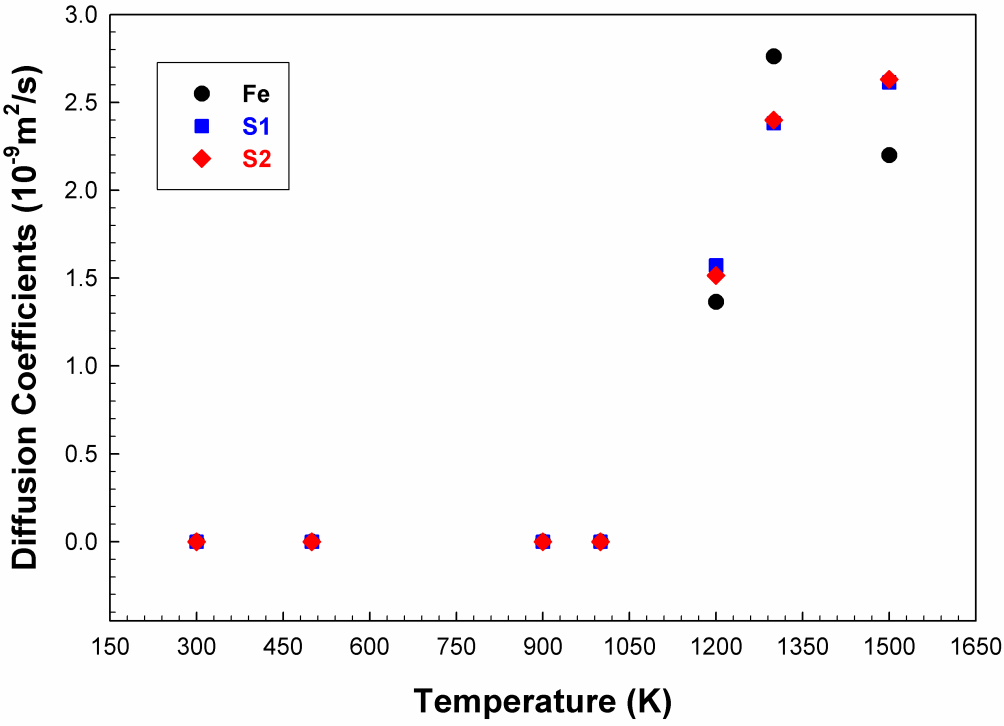

Figure 4.30: The graph of diffusion coefficient of ions Fe, S1, S2 as function of temperature for marcasite.

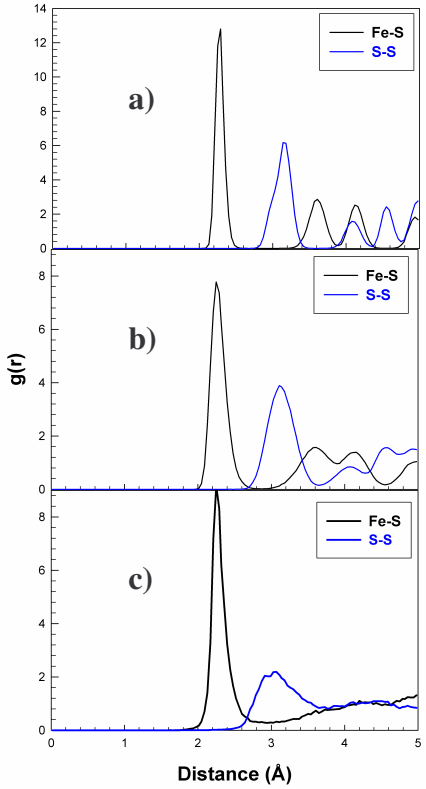

Figure 4.31: The radial distribution functions of marcasite at a) 300 K, b) 900 K and c) 1100 K.

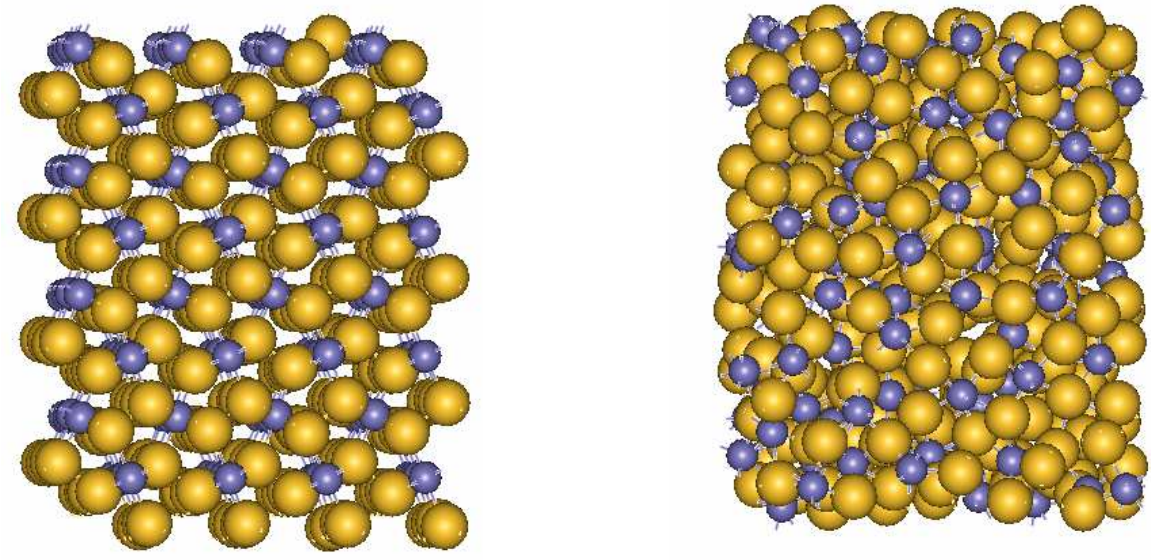

a) **b)**

Figure 4.32: The structure of the bulk at the temperatures a) 300 K and b) 1100 K.

Figure 4.32 shows the bulk atomic structure of marcasite at temperatures of 300 K and 1100 K. At 300 K the structure is well-ordered while at 1100 K the structure is disordered and amorphous which depicts melting at 1100 K.

4.6. {101} S Surface (Marcasite)

We study the most stable surface of marcasite {101}, terminated by sulphur. The simulation was performed in the same way as that of the bulk. Figures 4.33 a)-c) show the MSD of Fe, S1, S2 as a function of simulation time at 300 K, 900 K and 1100 K. It is obvious that the MSDs increase slightly with time; at 300 K and 900 K and it is enhanced at higher temperatures. Unlike in the bulk structure, the mobility of the ions on the surface is noticeable at a lower temperature of 900 K.

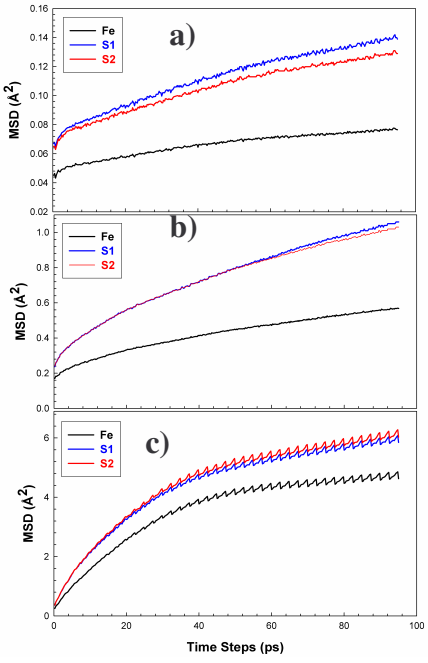

Figure 4.33: The mean squared displacement of all the ions, Fe, S1 and S2 at the temperatures of a) 300 K b) 900 K and c) 1100 K for marcasite.

At 1100 K, high values of MSDs are noted and the mobilities of sulphur ions are higher than that of iron. The melting on this surface is also reflected by the diffusion coefficient vs. temperature curve presented in Figure 4.34 where a substantial increase occurs above 1100 K.

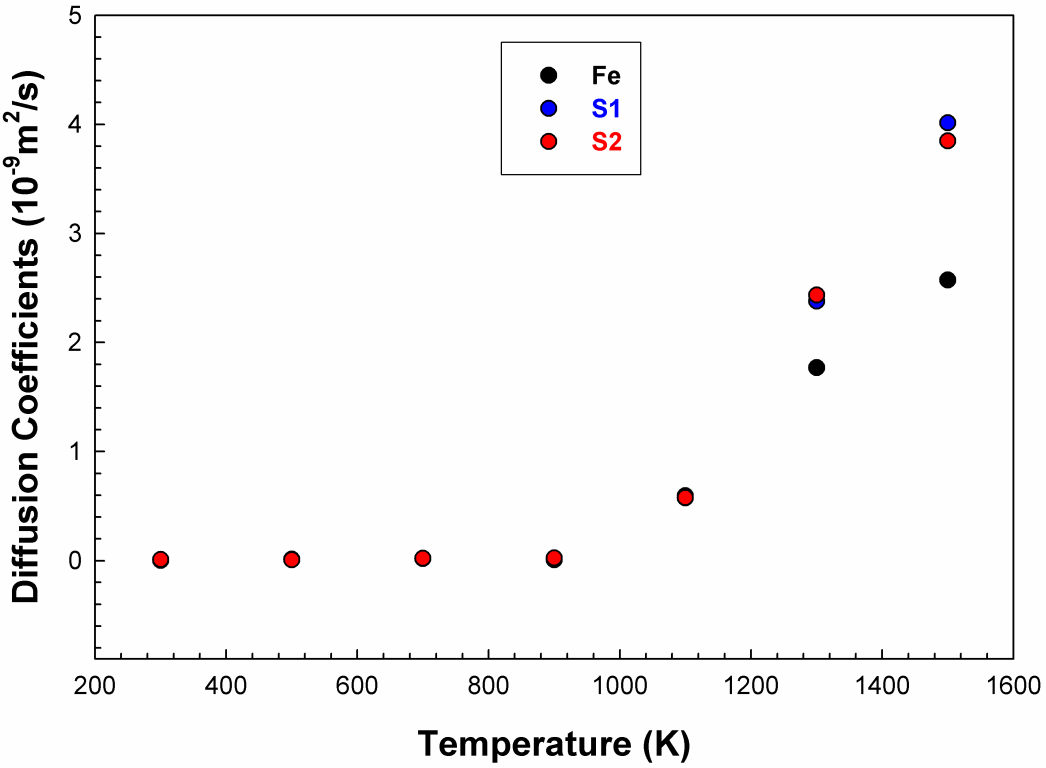

Figure 4.34: The graph of diffusion coefficient as function of temperature for {101} surface of marcasite.

In order to obtain detailed information on local structures in FeS_2 the radial distribution functions (RDFs) for all pairs of ions were calculated. Fe-S and S-S RDFs at the temperatures of 300 K, 900 K and 1100 K are shown in Figure 4.35 (a-c). At 300 K the surface has a well-ordered structure; and the RDFs have many peaks for both interactions. At 900 K the heights of peaks decreases and the signs of melting on the surface emerge at 900 K. The number of peaks especially for S-S has not changed significantly compared to those in the bulk.

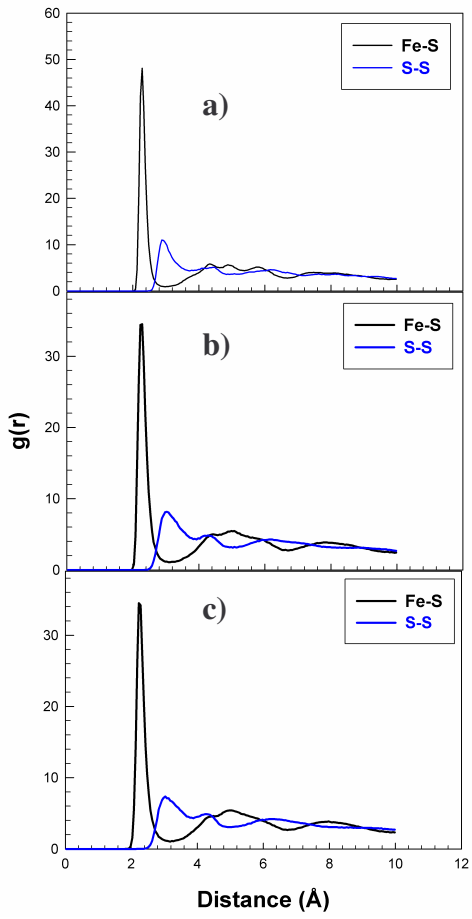

Figure 4.35: The radial distribution function graphs of marcasite at a) 300 K, b) 900 K and c) 1100 K.

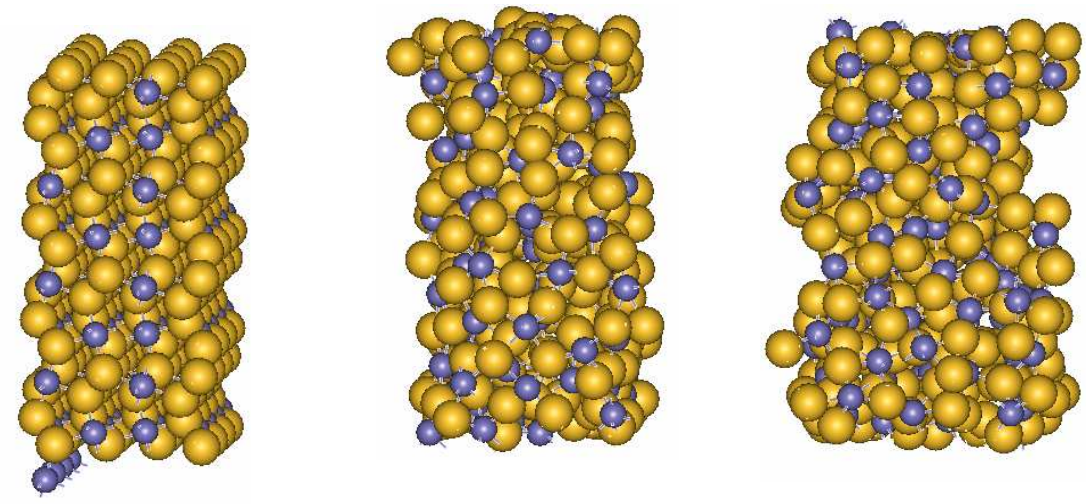

a) **b)** **c)**

Figure 4.36: The structures of the sulphur terminated {101} surface at temperatures of a) 300 K, b) 900 K, and c) 1100 K, in marcasite.

Figure 4.36 shows the structures of the sulphur terminated {101} surface at the temperatures of 300 K, 900 K and 1100 K. At 300 K (Figure 4.33a), the crystalline structure is maintained and significant disordered is noted at 900 K (Figure 4.33 b)). Figure 4.33 c) depicts that the {101} surface is in a liquid phase.

4.7 Conclusion

The surface energies for the {100}, {110} and {111} surfaces of pyrite were calculated as a function of temperature using molecular dynamics. The surface energies for each surfaces remained essentially constant up to the temperature of 1500 K. At the temperature of 1100 K the {100} S, {110} S, {111} S surfaces and the stepped surface {210} were disordered with appreciable amounts of diffusion of both the Fe, S1, S2 ions at the surface indicating the melting of the surface. As for the bulk, the disordering was observed at a temperature of 1300 K. We have noticed that the melting temperature of the surface is below that of the bulk. The reduction in the melting of the surface as compared to the bulk has been cited by Chen et al. (1990). It was possible to observe a phase transition from a solid phase to a liquid phase. The temperature at which the crystal melts for all surfaces terminated by sulphur is 1100 K. For the {100} surface terminated by iron the melting of the surface was also observed at 1100 K. This shows that the melting temperature of the surface is not affected by the termination of the surface. We have also studied the other FeS_2 polymorph, marcasite. We investigated the bulk and {101} surface, which is the most stable surface of marcasite.

We have calculated the surface energies using both the energy minimisation and molecular dynamics, and further studied the effect of water on the surfaces using

energy minimisation method. We noted that the surface energies of the dry surfaces are higher than those of hydrated surfaces. This implies that the hydration of the surfaces has a stabilizing effect on the pyrite surfaces.

Chapter 5

The structure of FeS_2 Nanocrystals

5.1. Aggregation of nanoparticles

One possible approach of simulating the nanoparticle aggregation is to use molecular dynamics. This serves the purpose of studying the structural changes that the nanoparticle undergoes during aggregation. This chapter describes the initial work on how MD may provide insights into the pathways of processes such as aggregation.

The big question is what makes these nanoparticles aggregate? Thus it is important to quantify the interactions of these nanoparticles. The classical Derjaguin-Landau-Vervey-Overbeek (DLVO) theory has been widely employed in colloid science to study particle-particle interactions, colloidal stability, coagulation, sedimentation, filtration and the behaviour of electrolyte solutions. The classical DLVO theory states that the total interaction potential between two nanoparticles (V_T) can be expressed as the sum of the electrostatic repulsion (V_{elec}) and the van der Waals attraction (V_{vdw}) [Lee et al. 1998 and Kim et al. 2005]

$$V_T = V_{elec} + V_{vdw} \qquad (4.1)$$

Van der Waals dispersive forces produce attractive interactions between bodies, playing an important role in many material systems influencing colloidal and emulsion stability, wetting behaviour, and intergranular forces in glass-ceramic systems. Hence, it is of technological importance to accurately quantify these interactions, conveniently represented by Hamaker constant, A (Ackler et al. 1996). The attractive van der Waals dispersion forces arise when dipoles interact across an

intervening medium. The van der Waals force has an electrodynamic origin as it arises from the interactions between atomic or molecular oscillating or rotating electrical dipoles within the interacting media (Bergstrom, 1997). Hamaker constants and the van der Waals interactions which they represent play a wide ranging role in the behaviour and interactions of materials (French et al., 1995). There are three types of interactions which contribute to the van der Waals force:

(i) The Keesom force which is the interaction between two permanent dipoles.

(ii) The Debye force which is the interaction between one permanent dipole and one induced dipole.

(iii) The London or dispersion force which is the interaction between two induced dipoles.

If the particles are spherical, the van der Waals attraction potential energy between two particles of radius a_1 and a_2 is:

$$V_{vdw} = -\frac{A}{6}\left[\frac{2a_1a_2}{R^2-(a_1+a_2)^2} + \frac{2a_1a_2}{R^2-(a_1-a_2)^2} + \ln\frac{R^2-(a_1+a_2)^2}{R^2-(a_1-a_2)^2}\right] \quad (4.2)$$

where A is the Hamaker constant and R is the distance between the centres of the two particles. The accurate estimations of the Hamaker constants are necessary for a quantitative understanding of the effect of interparticle forces on various phenomena (Bergstrom, 1997). Leong and Ong (2003) mentioned that the Hamaker constant is very difficult to quantify precisely and cannot be directly measured in a laboratory, it may be calculated from the Lifshitz theory of molecular attraction between macroscopic bodies.

The MD simulations was set up almost the same as that of the surface and bulk simulations. The initial calculation was performed with an eight nanoparticle system. Eight unrelaxed 1.5nm diameter nanoparticles are generated in a simulation cell of 2592 atoms so that each nanoparticle takes up a corner of the box. Each nanoparticle in the simulation is 1.7nm distance apart and they are identical to each other with a diameter of 1.5nm. The MD simulation was performed in vacuum, on a canonical ensemble (NVT) at the temperature of 300K and ambient pressure using time step of 0.1fs. Figure 5.1 shows the initial configuration of eight pyrite nanoparticles.

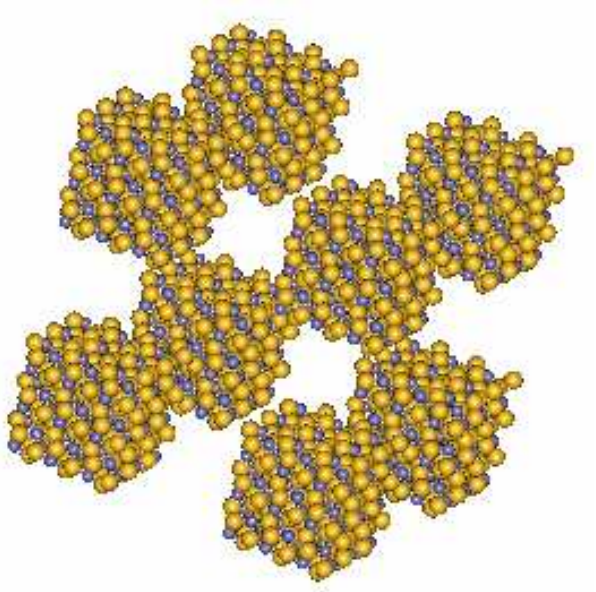

Figure 5.1: Initial configuration of pyrite nanoparticles for MD simulation

Our MD simulation was run for 300 picoseconds. Figure 5.2 shows the potential energy of the system as a function of MD time, where the initial value was $-28.950\times10^{3}eV$. As the simulation evolves we note the first drop around 70ps to the potential energy of $-28.966\times10^{3}eV$. The potential energy drops until it remains constant, which shows that all eight nanoparticles have aggregated.

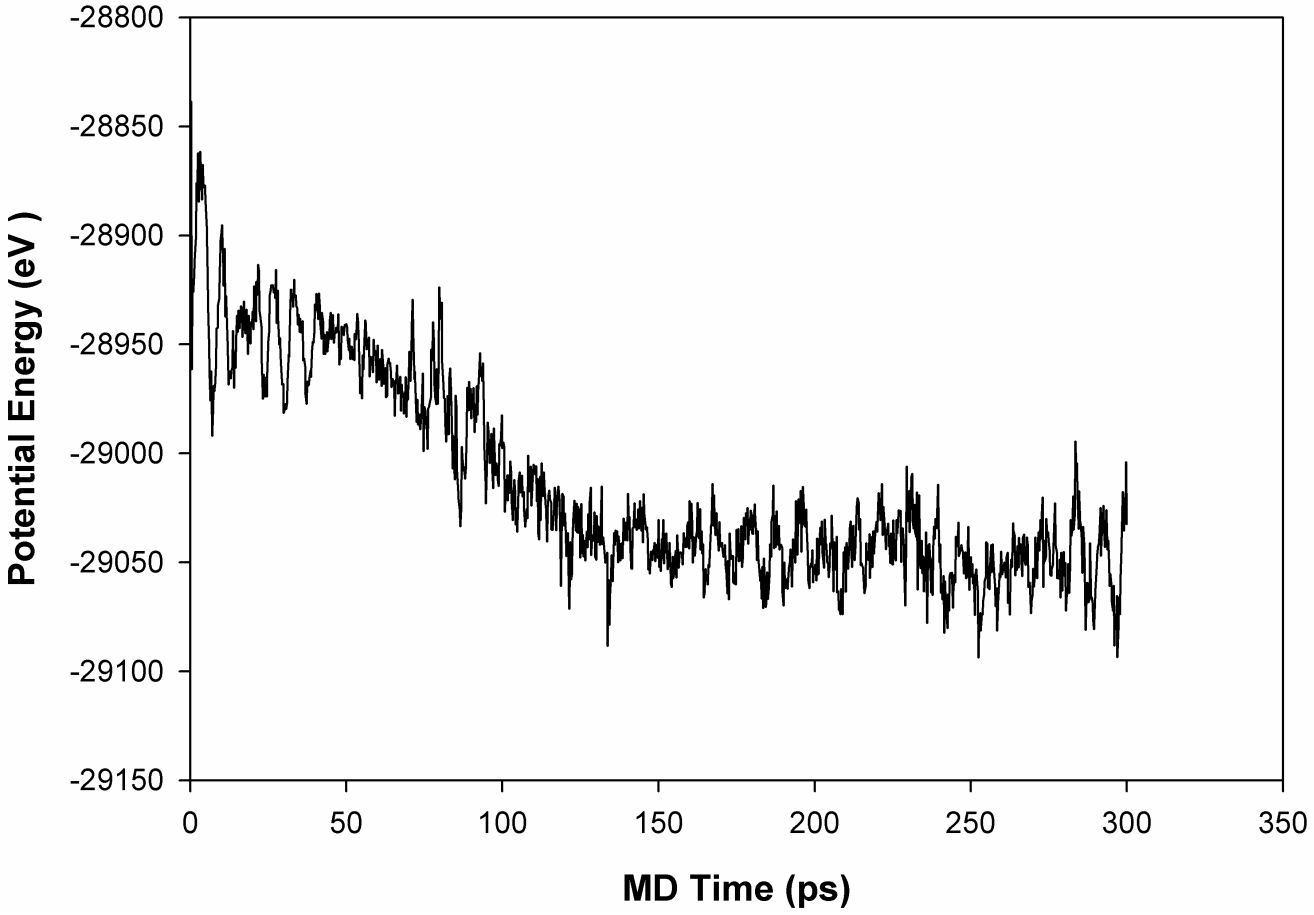

Figure 5.2: Evolution of potential energy of the aggregating pyrite nanoparticles with MD time

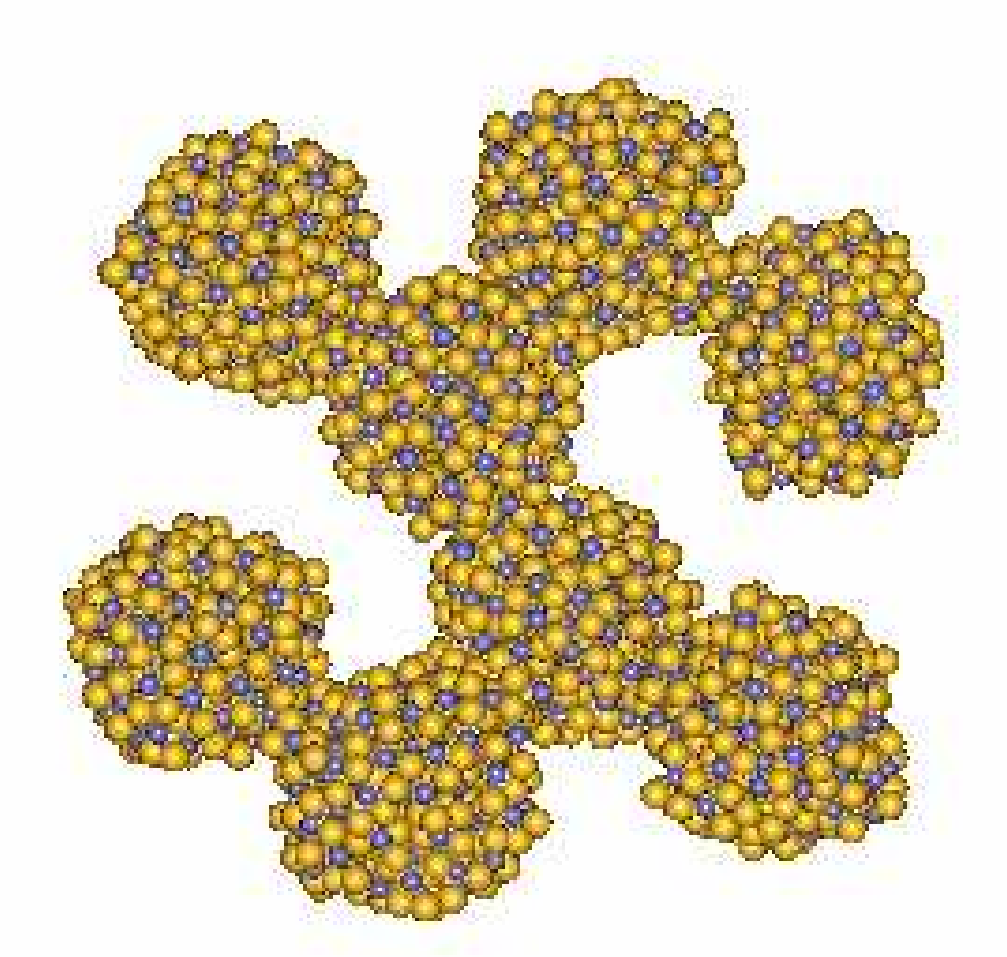

Figure 5.3: A snapshot of relaxed pyrite nanoparticles.

Figure 5.3 shows that before aggregation occurs the individual nanoparticles will relax on their own to a potential energy of around $-28.919\times10^{3}\,eV$. Once the pyrite particles are relaxed the particles come together one by one until they are aggregated. The particles adopt a near-amorphous structure. The final structure is shown in figure 5.4. The Hamaker constant was estimated to be $-3.0\times10^{-18}\,J$.

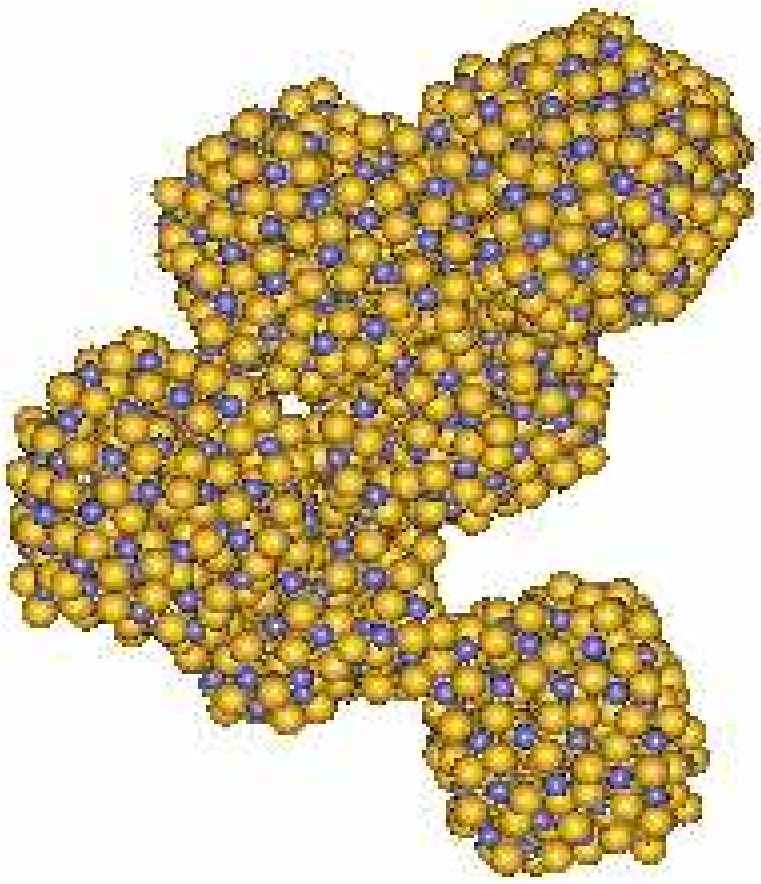

Figure 5.4: The final structure of aggregated pyrite nanoparticles

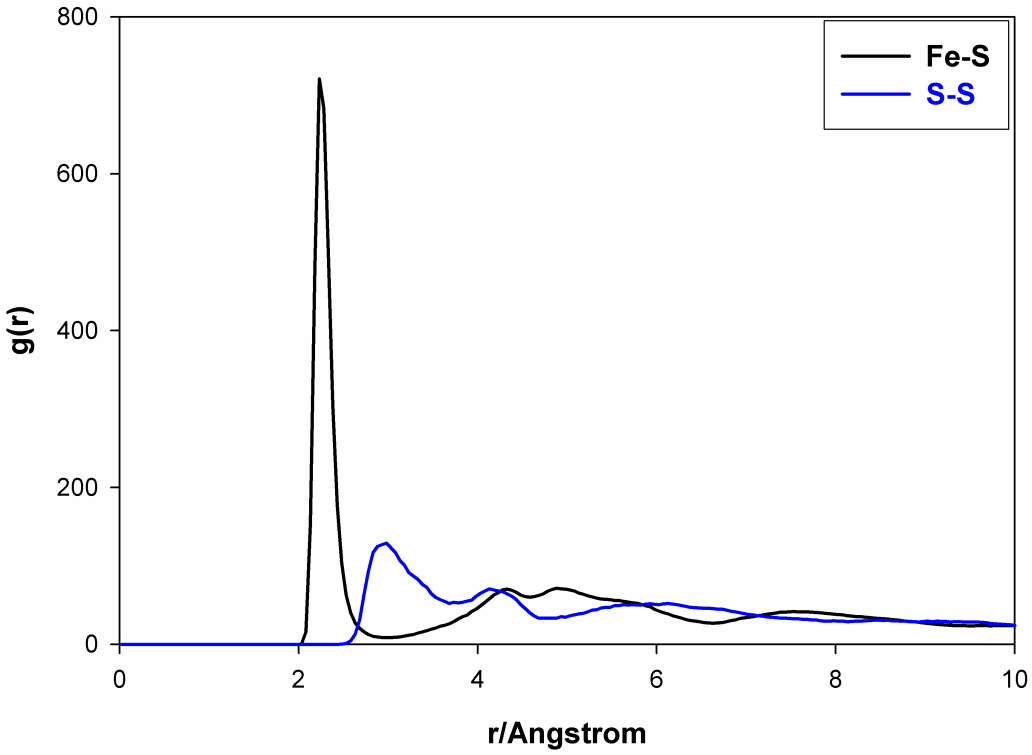

Figure 5.5: The RDFs of the aggregated pyrite nanoparticles

The RDFs of the aggregated structure also show that the structure is amorphous, as depicted by figure 5.5.

5.2. Effect of Water on the Structure of a Pyrite Nanoparticle

It is clear that such small FeS_2 nanoparticles are amorphous. The aim of this section is to ascertain whether immersing the particles in water would modify their structure. Molecular dynamics simulation was performed on the 1.5nm pyrite nanoparticle immersed in water in the NVT ensemble at room temperature, 300 K, and zero pressure. The simulation was run for 100 ps and the cubic simulation cell contained 1034 water molecules. Figures 5.6 and 5.7 show the structure of pyrite nanoparticle immersed in water and the initial nanoparticle, respectively.

To interpret our results we compared them with pyrite nanoparticle in vacuum and the bulk.

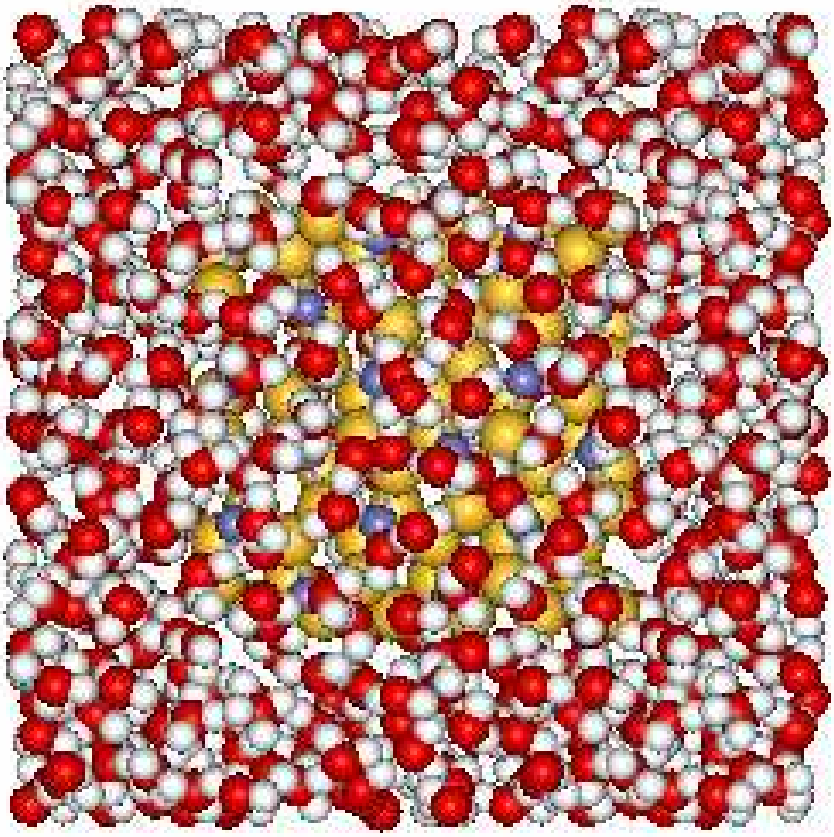

Figure 5.6: The structure of a pyrite nanoparticle immersed in water.

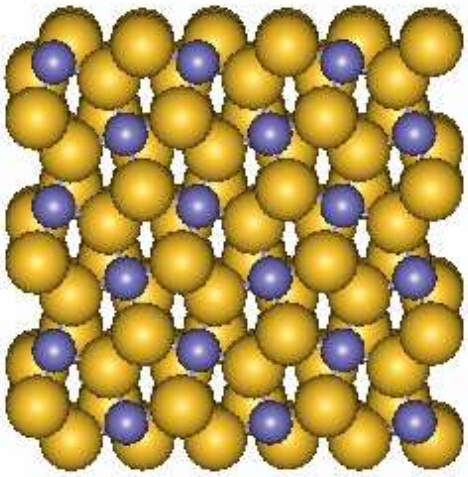

Figure 5.7: The initial configuration nanoparticle (removed water to show how the structure looks like before simulation)

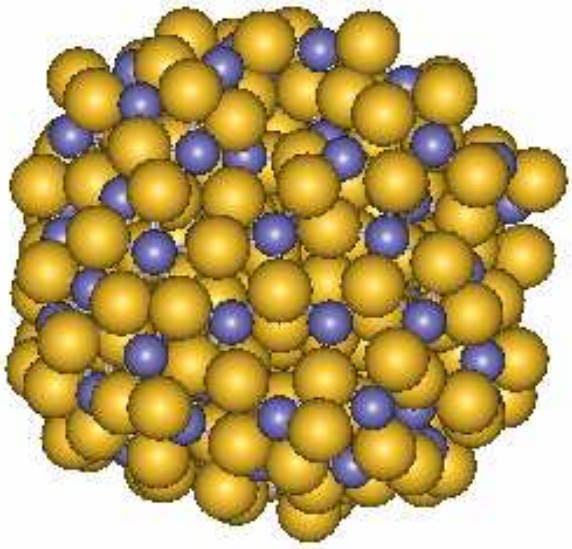

Figure 5.8: Nanoparticle in vacuum after simulation.

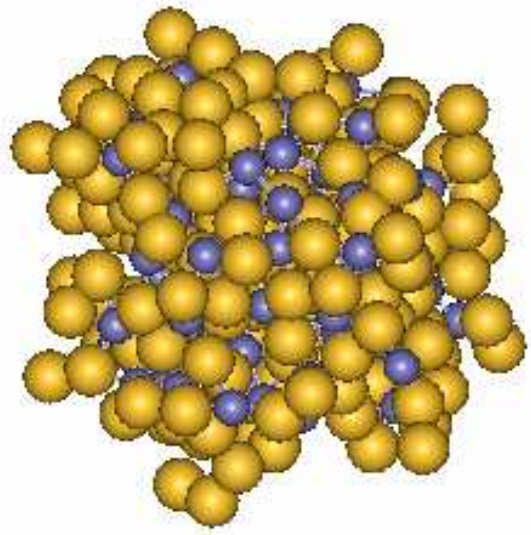

Figure 5.9: Nanoparticle in water (removed water for clarity) after simulation

Figures 5.7, 5.8, 5.9 show the snapshots of pyrite nanoparticle, in the initial configuration, in vacuum and water, respectively. The initial configuration shows the clear cubic structure. In vacuum, the nanoparticle has lost its cubic shape and the corners have smoothed out. For the one immersed in water, the nanoparticle adopts an intermediate structure. The radial distribution functions (RDFs) of both simulations for nanoparticle in water, vacuum and bulk are shown in figure 5.10(a)-(c). Figure 5.10(a) shows that the bulk has a well-ordered structure compared to nanoparticle in water (figure 5.10(c)), which shows that the structure has lost the crystallinity. For one nanoparticle in water the RDF peaks are not clearly separated as in the bulk RDF for both Fe-S and S-S interactions. The difference between the bulk and nanoparticle emanates from the fact that as the size of a material reduces to the nanometer scale the properties change uniquely in comparison with the bulk characteristics of the parent.

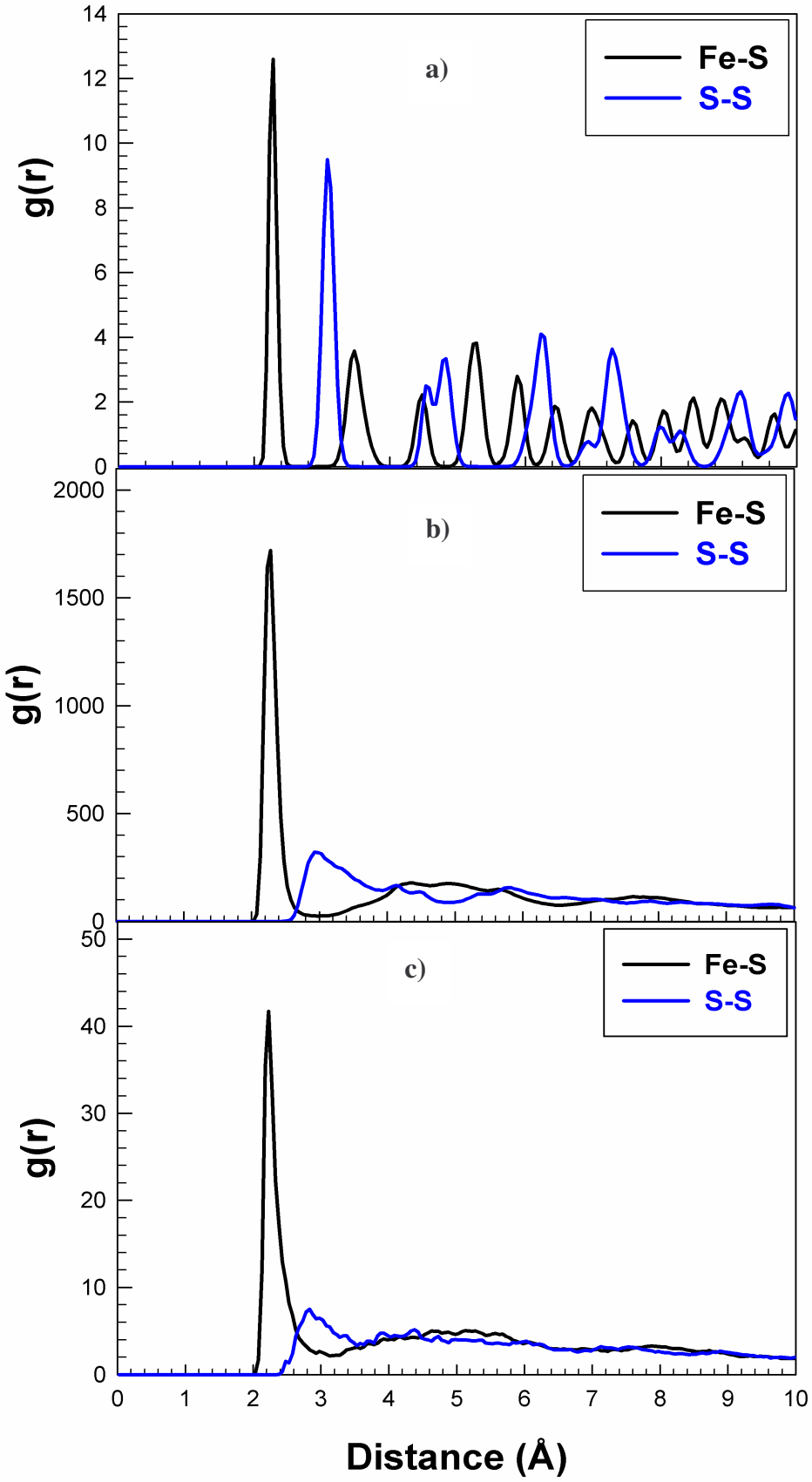

Figure 5.10: The RDFs of a) bulk, b) nanoparticle in vacuum and c) nanoparticle in water, for pyrite.

The origins of this may be attributed to the dimensions of the particles being comparable to the length scales of basic quanta in solids (i.e. mean free path of electrons, phonon wavelengths, coherency lengths) (Sayle et al. 2003). Comparing the RDFs of the nanoparticle in vacuum, figure 5.10(b), and in water, we notice that for both cases the RDFs are disordered. However, the water RDF is not as smooth as vacuum RDF. The water RDF have small peaks after the first peak, which are only just observable. This implies that the water induces some crystallisation, but not much for this size crystal. Kerisit et al, (2005) obtained the same results for calcite when they used molecular dynamics simulation to study the effect of water on a 1.5 nm nanoparticle and compared the results with the same particle in vacuum. Zhang et al, (2003) modelling a 3 nm nanoparticle of ZnS found that water did stabilise the crystal , although they observed a phase change and noted that the ZnS crystal structure was not the stable bulk structure.

5.4 Conclusion

The results of this study show that the pyrite particles adopt the near-amorphous structure. This is evident from a comparison of the RDFs of the bulk and those of aggregated nanoparticles. The RDFs of the bulk ions have many peaks and long range order as compared to the RDFs of aggregated structure, which does not reflect long range order. This study also shows that structural changes also emanate from changing the shape of nanometer-sized particles. Thus the MD simulations provide insights into factors governing aggregation in nanoparticles of FeS_2. We also considered a 1.5 nm pyrite nanoparticle in water and in vacuum and we found that the nanoparticle shows a much more amorphous structure in vacuum and in the presence of water the pyrite structure is stabilised. The next step is clearly to investigate

whether the particle size significantly modifies the crystallinity and structure of the nanoparticle. We have been able to quantify the aggregation of nanoparticles in vacuum, and provide an estimate of the Hammaker constant. Future work should consider how the solvent affects this value.

Chapter 6

Conclusion

We have successfully presented the atomistic simulation studies employing two techniques, i.e. energy minimization and molecular dynamics, to study the surfaces, {100}, {110}, {111} and {210} of pyrite FeS_2. The modified interatomic potentials of pyrite have been able to improve some of our parameters, e.g. S-S bond length, from the original potentials. The modified potentials have improved the stability of the most stable surface, {100} of pyrite. The original potentials gave the surface energy of 1.23 J/m^{-2} while the modified potentials gave 1.04 J/m^{-2}. We evaluated the effect of temperature on the surfaces and the bulk and in keeping with early predictions by Mott, we noted that the melting temperature of bulk is higher than that of surfaces. Furthermore, it is also structure specific; as an example we found that the melting temperature of {100} surface terminated by iron is higher than that of {100} surface terminated by sulphur. This is ascribed to the melting point of iron being experimentally very high as compared to the melting temperature of sulphur. We also studied the effect of water or hydration on the surfaces; which proved to have a stabilizing effect on the surfaces, again {100} surface is still the most stable surface. We have also studied the other FeS_2 polymorph, marcasite. We only investigated the bulk and {101} surface, which is the most stable surface of marcasite. For the bulk marcasite diffuse at the temperature of 1100 K while for the {101} surface start at 900K.

We have also studied the nanocrystals of pyrite; where the aggregation of nanoparticles of pyrite and the effect of water on a pyrite nanoparticle were

considered. The aggregation of nanoparticles showed that the particles adopt the near-amorphous structure. We also proved that a pyrite nanoparticle shows a more amorphous structure in the presence of water, but in vacuum water stabilized the pyrite structure.

As for future work, we will study the effect of different surfactants, such as methanoic acid, methylamine, hydroxyethanal, hydroxamic and even xanthate on the surface structures and stabilities of pyrite.

References

Ackler H.D., French R.H., and Chiang Y.M., J. Colloid and Interface Sci., **179**, 469, 1996

Allen, M.P., Tildesley, D.J., *Computer Simulation of Liquids* (Oxford Scientific Publishing, Oxford, UK, 1987).

Baker B.J, and Banfield J.F. FEMS Microbiol. Ecol., **44**, 139, 2003

Bergstrom L, Adv. Colloid Interface Sci. , **70**,125, 1997

Born, M.; and Huang, K. *Dynamical Theory of Crystal Lattices*; Oxford University Press: Oxford, 1954.

Cai J. and Philpott M.R., Computat. Mat. Sci**, 30**, 358, 2004

Catlow C. Richard A, Computer modelling as a technique in solid state Chemistry, Faraday Discussion, 1997, **106**, 1È40

Chen E.T., Barnett R.N. and Landman U. Phys. Rev. B**41**, 439, 1990

Chen S.H., Tsay M.Y., Huang and Yu J.T., J. Phys. Condens. Matter**. 6**, 9211, 1994

Chen S.H., Tsay M.Y., Huang Y.S. and Yu J.T., J. Phys.: Condens. Matter. **6**, 9211, 1994.

Chen X., Wang Z., Wang X., Wan J., Liu J., Qian Y., Inorganic Chemistry, **44**, 951, 2005

Chin P.P., Ding J., Yi J.B. and Liu B.H., J. Alloys and Compounds, **390**, 255, 2005

Cooke D.J., PhD Thesis, University of Bath, 2003.

De Leeuw N.H. and Parker S.C, Phys. Rev. B, **58**, 13901, 1998a

De Leeuw, N.H. and Parker S.C, J. Phys. Chem. B **102**, 2914, 1998b.

De Leeuw N.H. and Parker S.C., Mol. Sim., **24**, 77, 2000

De Leeuw N.H., Parker S.C, and Catlow C.R.A, and Price G.D, Phys. Chem. Minerals, **27**, 332, 2000.

Deer, W.A., Howie R.A., and Zussman J., *An introduction to the Rock-forming Minerals* 2nd edition, Prentice Hall, 1992.

Descostes M., Vitorge P. and Beaucaire C., Geochimica et Cosmochimica Acta, Vol. **68**, 4559, 2004.

Elsetinow A.R., Guevremont J.M., Strongin D.R., Schoonen M.A.A. and Strongin M., Am. Mineralogist, **85**, 623, 2000.

Eneroch E. and Koch C.B., Minerals Engineering, **16**, 1257, 2003

Eyert V, Hock K.H., Fiechter S, and Tributsch H., Phys. Rev., B**57**, 6350, 1998.

Fisler D.K., Gale J.D., and Cygan R. T., Am. Mineralogist, **85**, 217, 2000.

French R.H., Cannon R.M., DeNoyer L.K., and Chiang Y.M., Solid State Ionics, **75**, 130, 1995.

Frenkel, D., Smit, B., *Understanding Molecular Simulations: from Algorithms to Applications* Academic Press; San Diego, 1996.

Fullerton S.K., Maranas J.K., NANOLETTERS, **l5**, 363, 2005

Henderson M.A., Surf. Sci. Reports, **46**, 1-308, 2002.

Higgins K. J, Jung H, Kittelson D.B, Roberts J.T, and Zachariah M.R., J. Phys. Chem., A**106**, 96, 2002

Holender J.M, Phys. Rev., B**41**, 8054, 1990.

Hopfner C., Ellmer K., Ennaoui A., Pettenkofer C., Fiechter S. and Tributsch H., J. Cryst. Growth, **151**, 325, 1995

http://www.gamineral.org/pyrite.htm

http://www.reade.com/Products/Sulfides/Iron_Sulfide.html

Huang Y.S., Huang J.K., and Tsay M.Y.; J. Phys.: Condens. Matter, **5**, 7827, 1993

Hung A, Muscat J, Yarovsky I, Russo S.P.; Surf. Sci., **513**, 511, 2002a

Hung A, Muscat J, Yarovsky I, Russo S.P.; Surf. Sci., **520**, 111, 2002b

Hung A., Yarovsky I. and Russo S.P., J. Chem. Phys., **118**, 6022, 2003

Kerisit S., Cooke D.J., Spagnoli D., Parker S.C., J. Mat. Chem., **15**, 1454, 2005.

Kerist S. N., PhD Thesis, University of Bath, 2005.

Kim T, Lee K, Gong M. and Joo S., Langmuir, **21**, 9524, 2005.

Kjekshus A. and Rakke T., Acta Chemica Scandinavica, A**29**, 443, 1975

Kob W., J. Phys.: Condens. Matter, 11, R**85**, 1999

Lee K, Sathyagal A.N., and McCormick A.V., Colloids and Surfaces A: Physicochemical and Engineering Aspects, **144**, 115, 1998.

Leong Y.K. and Ong B.C., Powder Technology, **134**, 249, 2003.

Mattila S., Leiro J.A. and M. Heinonen, Surf. Sci., **566**, 1097, 2004

Meng L., Liu Y.H., Tian L., J. Cryst. Growth, **253**, 530, 2003

Mkhonto D, PhD Thesis, University of Limpopo, 2005.

Mock J.J., Barbic M., Smith D.R., Schultz D.A. and Schultz S., J. Phys. Chem., **116**, 6755, 2002

Muscat J, Hung A, Russo S, and Yarovsky I, Phys. Rev., B**65**, 054107, 2002

Oliver P.M., Watson G.W., Parker S.C., Phys. Rev., B**52**, 5323, 1995.

Parker S.C, De Leeuw N.H, and Redfern S.E, faraday Discussions, **114**, 381, 1999.

Qiu G., Xiao Q., Hu Y., Qin W., Wang D.; J. Colloid and Interface Sci., **270**, 127, 2004

Rath R. K., Subramanian S.; and Pradeepy T.; J. Colloid and Interface Sci. **229,** 82, 2000

Rosso K.M., Becker U. and Hochella Jr. M. F., Am. Mineralogist, **84**, 1549, 1999

Rosso K.M., Becker U. and. Hochella Jr. M. F., Am. Mineralogist, **84**, 1428, 2000

Sasaki Y., Suguii A., Ishii K., J. Mat. Sci. Letters, **18**, 193, 1999

Sayle D.C. and Parker P.C., J. Am. Chem. Soc., **125**, 8581, 2003

Sayle D.C., Doig J.A., Maicaneanu S.A, and Watson G.W., Phys. Rev., B**65**, 245414, 2002.

Sayle D.C., Doig J. A, Parker S.C., and Watson G. W., J. Mat. Chem., **13**, 2078, 2003.

Sithole, H.M., Ngugen-Manh, D., Pettifor, D.G., and Ngoepe, P.E., Mol. Sim., **22**, 31, 1999.

Tasker P.W., The stability of ionic crystal surfaces, J. Phys. C: Solid State Phys., **12**: 4977, 1979.

Tlali S.B., Mathe B.A., Kotane L.M., Schoning F.R.I., Comins J.D., Every A.G, Sithole H.M., Ngoepe P.E. and Wright K.V., Phys. Stat. Sol. (C) 1, 3073, 2004.

Verble J.L. and Wallis R.F., Phys. Rev., **182**, 1969

Wan D., Wang Y., Wang B., Ma C., Sun H., and Wei L., J. Cryst. Growth, **253**, 230, 2003

Watson G.W., Kelsey E.T., de Leeuw N.H., Harris D.J. and Parker S.C., J. Chem. Soc., Faraday Trans., **92**, 433, 1996.

Wu R., Zheng Y.F., Zhang X.G., Sun Y.F., Xu J.B. and Jian J.K., J. Cryst. Growth, **266**, 523, 2004.

Zachariah M.R. and Carrier M.J., and Blaisten-Barojas E., J. Phys. Chem., **100**, 14856, 864, 1996

Zeng Y. and Holzwarth N.A.W. , Phys. Rev. B **50**, 8214., 1994

Zhang H., Haung F., Gilbert B., Banfield J.F., J. Phys. Chem., B, **107**, 13051, 2003.

Zhang, H., and Banfield, J.F., NANOLETTERS, **4**, , 713, 2004

Appendix A

Papers and Posters Presented at Local and International Conferences

1. Computational Modelling of Transitional Metal Sulphides, InterScience conference, University of Limpopo, Turfloop Campus, (2003).

2. Computational Modelling of Transitional Metal Sulphides, Materials Modelling Science, University of Limpopo, Turfloop Campus, (2004).

3. Computational Modelling of Transitional Metal Sulphides, South African Institute of Physics (49^{th}), University of Free State, (2004).

4. Molecular Dynamics Simulation of Transitional Metal Sulphides (FeS_2), 3^{rd} South West Computational Chemistry Meeting, University of Bath, UK, (2004)

5. Computer Simulation of the effect of temperature on the pyrite (FeS_2), RSC Solid State Group Christmas Meeting, University of Birmingham, UK, (2004)

6. Atomistic modelling of the structure of FeS_2 (Pyrite), Materials Modelling Meeting, University of Limpopo, Turfloop Campus, (2005).

7. Atomistic modelling of the structure of FeS_2 (Pyrite), South African Institute of Physics (50^{th}), University of Pretoria, (2005)